New Journal of Physics
The open access journal at the forefront of physics

Deutsche Physikalische Gesellschaft DPG IOP Institute of Physics

PAPER • OPEN ACCESS

Relativistic aspects of orbital and magnetic anisotropies in the chemical bonding and structure of lanthanide molecules

To cite this article: Eite Tiesinga *et al* 2021 *New J. Phys.* **23** 085007

View the article online for updates and enhancements.

You may also like

- CEWQO Topical Issue
Mirjana Bozic and Margarita Man'ko
- First-principles calculations of hydrogen interactions with nickel containing a monovacancy and divacancies
Nishith K Das, Tetsuo Shoji, Takeharu Nishizumi et al.
- Focus on Cold Atoms in Optical Lattices
Immanuel Bloch and Peter Zoller

This content was downloaded from IP address 74.96.185.181 on 06/12/2021 at 19:13

New Journal of Physics
The open access journal at the forefront of physics

Deutsche Physikalische Gesellschaft DPG
IOP Institute of Physics

Published in partnership with: Deutsche Physikalische Gesellschaft and the Institute of Physics

OPEN ACCESS

RECEIVED
23 May 2021

REVISED
26 July 2021

ACCEPTED FOR PUBLICATION
4 August 2021

PUBLISHED
23 August 2021

Original content from this work may be used under the terms of the Creative Commons Attribution 4.0 licence.

Any further distribution of this work must maintain attribution to the author(s) and the title of the work, journal citation and DOI.

PAPER

Relativistic aspects of orbital and magnetic anisotropies in the chemical bonding and structure of lanthanide molecules

Eite Tiesinga[1,*], Jacek Kłos[2,3], Ming Li[2], Alexander Petrov[2,4] and Svetlana Kotochigova[2]

[1] Joint Quantum Institute, National Institute of Standards and Technology and the University of Maryland, MD 20899, United States of America
[2] Physics Department, Temple University, Philadelphia, PA 19122, United States of America
[3] Joint Quantum Institute, Department of Physics, University of Maryland, College Park MD 20742, United States of America
[4] Saint Petersburg NRC, Kurchatov Institute PNPI, Gatchina, 188300, Russia and Division of Quantum Mechanics, Saint Petersburg University, 199034, Russia
[*] Author to whom any correspondence should be addressed.

E-mail: eite.tiesinga@nist.gov

Keywords: ultracold lanthanide atoms, relativistic electronic structure, spin tensor decomposition, lanthanide molecules

Abstract

The electronic structure of magnetic lanthanide atoms is fascinating from a fundamental perspective. They have electrons in a submerged open 4f shell lying beneath a filled 6s shell with strong relativistic correlations leading to a large magnetic moment and large electronic orbital angular momentum. This large angular momentum leads to strong anisotropies, i. e. orientation dependencies, in their mutual interactions. The long-ranged molecular anisotropies are crucial for proposals to use ultracold lanthanide atoms in spin-based quantum computers, the realization of exotic states in correlated matter, and the simulation of orbitronics found in magnetic technologies. Short-ranged interactions and bond formation among these atomic species have thus far not been well characterized. Efficient relativistic computations are required. Here, for the first time we theoretically determine the electronic and ro-vibrational states of heavy homonuclear lanthanide Er_2 and Tm_2 molecules by applying state-of-the-art relativistic methods. In spite of the complexity of their internal structure, we were able to obtain reliable spin–orbit and correlation-induced splittings between the 91 Er_2 and 36 Tm_2 electronic potentials dissociating to two ground-state atoms. A tensor analysis allows us to expand the potentials between the atoms in terms of a sum of seven spin–spin tensor operators simplifying future research. The strengths of the tensor operators as functions of atom separation are presented and relationships among the strengths, derived from the dispersive long-range interactions, are explained. Finally, low-lying spectroscopically relevant ro-vibrational energy levels are computed with coupled-channels calculations and analyzed.

1. Introduction

A challenging question of molecular chemistry is an accurate description of inter-atomic and inter-molecular bonding at the quantum-mechanical level. This problem has attracted much attention but is not always resolved. Over the last decades, novel perspectives on the problem have relied on ultracold atoms and molecules. For example, quantum degenerate gases of atoms offer a unique platform on which to build and form small molecules in single internal state as they avoid unwanted system complexity. Ultracold gasses of atoms and molecules typically also allow for a high level of control and tunability and are well isolated from their surroundings.

As part of these developments experimental breakthroughs in realizing quantum gases of atoms with large magnetic moments [1–9] have also contributed. These atomic species tend to have a far more complex electronic structure than that of alkali-metal or alkaline-earth species most often studied in the field. The

© 2021 The Author(s). Published by IOP Publishing Ltd on behalf of the Institute of Physics and Deutsche Physikalische Gesellschaft

magnetic lanthanides from dysprosium to thulium with their exceptionally large magnetic moments and large orbital momenta are extreme examples of such species. This experimental research relied on controllable and tunable anisotropic dipolar interactions between the atoms. The highly anisotropic short-range interactions between lanthanide atoms, however, remain poorly understood as they require knowledge of their chemical bonds. These systems form an excellent environment for explorations at the interface between quantum chemistry and atomic and molecular physics.

In previous research, we developed a successful model Hamiltonian to study the anisotropic interactions of bosonic Dy and Er in an external magnetic field [10, 11] and in collaboration with the experimental groups of Drs Ferlaino and Pfau we found and analyzed hundreds of magnetic Feshbach resonances in their collisions [12–14]. These resonances can be used to convert an atomic gas into a gas of highly-magnetic molecules as well as to study the threshold properties or the ultracold collision-energy dependence of three-body relaxation [15]. These atom–atom interactions have also been studied in thulium (Tm) [16, 17].

In spite of advances in the simulation of ultracold collisional interactions between heavy lanthanide atoms, the fundamental nature of the relativistic bond and short-range electronic states in lanthanide dimers as well as in the even-heavier actinide dimers remains mostly unexplored. Precise knowledge of these interactions is clearly desirable for predicting their quantum vibrations and rotations. There exists an exception though. Substantial progress has been made in understanding interaction in the homonuclear diuranium molecule U_2 [18–21]. The latest studies [20, 21] paid particular attention to the chemical bond of U_2 with its multi-orbital character. Relativistic and correlation effects using the Dirac equation for the electrons were fully incorporated by the authors of reference [21] and enabled them to determine the energies of the lowest electronic states of U_2 in the vicinity of the equilibrium separation. In addition, accurate ground-state potentials for heteronuclear dimer molecules that include one open 4f-shell lanthanide atom and one non-lanthanide atom have become available [22–28].

The bond between two ground-state Er and two ground-state Tm atoms is the focus of this paper. The interactions between the $j = 6$ Er atoms and between the $j = 7/2$ Tm atoms are anisotropic and orientation dependent. Here, j is the total electron angular momentum of an atom. The anisotropy is a consequence of potential energy differences for different relative orientations of the electron angular momenta in the open $4f^{12}$ and $4f^{13}$ shells of Er and Tm, respectively. These 4f electrons lie beneath a closed $6s^2$ shell so that these molecules are chemically similar but have distinct physical properties. Electron motion in lanthanides is strongly correlated and relativistic and spin–orbit coupling is strong.

The ground-state manifold of Er_2 and Tm_2 has a large number of electronic states. They are labeled by projection quantum number Ω with values up to $2j$ of the total dimer electron angular momentum on the symmetry axis of the molecule and well as other selection quantum numbers. Because of this complexity, the intermolecular interactions until now have not been accurately characterized. To fulfill these objectives we have performed, for the first time, relativistic configuration-interaction calculations of all Ω states as a function of interatomic separation R for Er_2 and Tm_2 using the DIRAC code [29]. These configuration-interaction calculations determine the short-range energy splittings among the 91 and 36 distinct adiabatic potentials of the Er_2 and Tm_2 dimers, respectively.

Furthermore, we have setup an analytical spin-coupling or spin-tensor representation of the short-range electronic potential surfaces for their use in determining rotational-vibrational levels in this paper and future improved simulations of the scattering of ultra-cold Er and Tm atoms. This representation has seven spin tensor operators and follows from the analytic form of the long-range anisotropic dispersion or van-der-Waals interaction. We find that the splittings among the Er_2 and Tm_2 potentials are dominated by a single anisotropic dipolar coupling between one of the atomic angular momenta and the mechanical rotation of the atom pair. We have also computed the long-range coupling strengths for the seven tensor operators based on all known atomic transition energies and transition dipole moments of Er and Tm. In fact, we find simple relationships among the seven spin-tensor operators contributing to the long-range interaction Hamiltonian.

Finally, we predict the relativistic Hund's case (c) structure of the energetically-lowest rotational-vibrational levels of the homonuclear Er_2 and Tm_2 dimers using a discrete-variable representation for the vibrational motion. We hope that our predictions will pave the way to spectroscopic studies of these complex and interesting molecules in the near future.

2. Results and discussion

2.1. Ground electronic states of Er_2 and Tm_2

In this section we provide the relevant information on molecular electronic properties for two homonuclear lanthanide molecules, Er_2 and Tm_2, using a two-step approach to determine short-range electronic

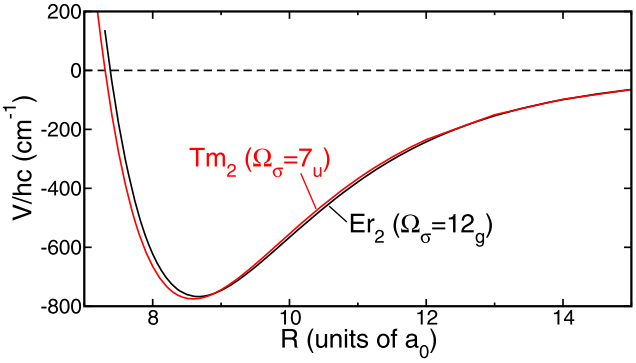

Figure 1. Potential energies of the energetically-lowest 'spin-stretched' states of Er_2 (black curve, $\Omega_\sigma = 12_g$) and Tm_2 (red curve, $\Omega_\sigma = 7_u$) as functions of internuclear separation R. The calculations are based on non-relativistic configuration-interaction and non-relativistic coupled-cluster theory for Er_2 and Tm_2, respectively. The zero of energy is at the dissociation limit of two ground-state atoms.

potential surfaces for all molecular states that dissociate to Er or Tm atoms in the electronic ground states $[Xe]4f^{12}6s^2(^3H_6)$ and $[Xe]4f^{13}\,6s^2(^2F_{7/2})$, respectively. These electronic configurations contain partially-filled or open submerged 4f and chemically-active 6s atomic orbitals. Computational details and justification of the two step process are presented in section 3 as well as the appendices.

In the first step of our study, we focus on the spin-stretched states of Er_2 with $\Omega_\sigma = 12_g$ and Tm_2 with $\Omega_\sigma = 7_u$, where subscripts $\sigma = g$ and u for *gerade* or *ungerade* indicate the inversion symmetry of the electron wavefunction with respect to the center of charge. These states have the maximum allowed total electron spin quantum number S and the maximum projection quantum number Λ of the total electron orbital angular momentum along the internuclear axis, corresponding to the $S = 2, \Lambda = 10$ and $S = 1, \Lambda = 6$ states for Er_2 and Tm_2, respectively. We have used non-relativistic configuration-interaction or coupled-cluster calculations to determine an accurate depth for the potential energy of these spin-stretched states.

Figure 1 shows the spin-stretched potential energy curves for Er_2 and Tm_2 as functions of interatomic separation R. The relatively shallow potential depths of just under $hc \times 800$ cm^{-1} reflect the covalent bond of the two closed $6s^2$ orbitals. The equilibrium separations at the potential minima are $R_e = 8.7a_0$ and $8.6a_0$ for Er_2 and Tm_2, respectively. Here, h is Planck's constant, c is the speed of light in vacuum, and $a_0 = 0.052\,9177$ nm is the Bohr radius. The depth and shape of these potentials is similar to that of the $X^1\Sigma_g^+$ state of the non-magnetic Yb_2 [30].

In a second step, we determine energy splittings among the Er_2 and Tm_2 potentials, using fully-relativistic configuration-interaction method implemented into DIRAC 2019 [29] that includes spin–orbit and anisotropic short-range interactions between atoms with two open 4f shells. The states are described by the projection quantum number of the total electronic angular momentum $\vec{J}_{el} = \vec{J}_1 + \vec{J}_2$ on the internuclear axis Ω, the *gerade* and *ungerade* symmetry, and a parity symmetry for $\Omega = 0$ states. Here, Ω ranges from 0 to 12 for Er_2 and 0 to 7 for Tm_2 and labeling $\Omega^\pm = 0^+$ or 0^- indicates a symmetry with respect to the reflection of the electron wavefunction through a plane containing the internuclear axis.

Figures 2(a) and (c) show the *gerade* relativistic potential energy surfaces (PESs) for Er_2 and Tm_2 as functions of internuclear separation near their equilibrium separation. There are 49 *gerade* potentials for Er_2 and 16 for Tm_2. For the separations shown in the figure and, in fact, for larger separations the splittings are less than 10 % of the depth of the potentials relative to the dissociation energy. The figures for the *ungerade* states is qualitatively similar and reproduced in the appendices. There are 42 and 20 *ungerade* potentials for Er_2 and Tm_2, respectively.

The splittings among the *gerade* relativistic potentials seem at first glance nontrivial. A pattern, however, emerges when we plot the potential energies at a single R near the equilibrium separation as functions of projection quantum number Ω, see figures 2(b) and (d). For both dimers the energetically lowest potential is a 0_g^+ state. We also observe that the splittings among states with the same Ω gradually decrease with increasing Ω. In fact, the potential energies at the equilibrium separation are arranged in parabolic shapes. Finally, for Er_2 the 0_g^+ state with the smallest well depth is nearly degenerate with the spin stretched 12_g state. A discussion of the origin of this pattern is given in the following subsection. Please note that the $\Omega = 7$ state for Tm_2 has *ungerade* symmetry.

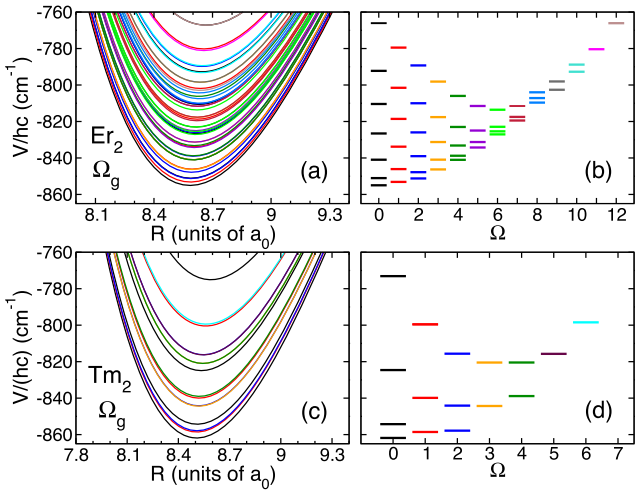

Figure 2. Relativistic $\Omega_g^{\pm}$ potential energy curves with *gerade* symmetry for Er_2 (panel a) and Tm_2 (panel c) as functions of internuclear separation R near the equilibrium separation as obtained from electronic structure calculations. All potentials approach zero energy for $R \to \infty$. Panels (b) and (d) show potential energies from panels (a) and (c) using the same line colors at the equilibrium separation as functions of projection quantum number Ω for Er_2 and Tm_2, respectively. *Gerade* $\Omega = 0$ states are 0^+ states. Potentials of states with Ω and $-\Omega$ are degenerate.

2.2. Spin tensor decomposition of Er_2 and Tm_2 PESs

A tensor decomposition of the PESs enables us to write PESs as weighted sums of spin-spin coupling terms. It removes the need for a complicated evaluation of non-adiabatic couplings among potentials. We believe that the tensor format is essential for our molecular systems with their tens to hundred adiabatic channel potentials in the ground configuration.

Here, we apply the tensor decomposition technique developed in our previous study of scattering dynamics between ultracold Dy atoms [10] assuming that the molecular electronic wavefunction is well represented by superpositions of (anti-)symmetrized, parity-conserving products of atomic electronic ground states $|j_i m_i\rangle$ or $|j_i \Omega_i\rangle$ for atom $i = 1, 2$. Atomic states are labeled by eigenvalues of the total electronic angular momentum operator $\vec{j}_i$, where projection quantum numbers along a space-fixed quantization axis are denoted by m_i and those along the body-fixed internuclear axis by Ω_i. For homonuclear systems $j_1 = j_2 \equiv j$. Nevertheless, subscripts 1 and 2 on operators $\vec{j}_i$ and atomic states are kept to indicate the appropriate atom. (As always we omit the reduced Planck constant $\hbar$ in describing the eigenvalues of angular momentum operators.)

The atom-atom interactions are then expressed as a sum of isotropic and anisotropic spin-tensor interactions. In principle, an infinite number of such interactions of ever increasing complexity exist. We, however, only include the seven low-rank tensors that describe the van-der-Waals interaction at large interatomic separations [10]. These are

$$V(\vec{\mathbf{R}}) = \sum_{k=0,2,4} \sum_{i=1}^{N_k} V_k^{(i)}(R) \sum_{q=-k}^{k} (-1)^q T_{kq}^{(i)} C_{k,-q}(\hat{\mathbf{R}}) \tag{1}$$

with rank-k spherical tensor operators $T_{kq}^{(i)}$ with components q, spherical harmonic functions $C_{kq}(\hat{\mathbf{R}})$ with $C_{kq}(\hat{\mathbf{0}}) = \delta_{q0}$, and $\hat{\mathbf{R}}$ is the orientation of the interatomic axis. Here, δ_{ij} is the Kronecker delta. The seven $T_{kq}^{(i)}$ correspond to three isotropic rank-0 tensors

$$\hat{T}_{00}^{(1)} = I, \tag{2}$$

$$\hat{T}_{00}^{(2)} = [j_1 \otimes j_2]_{00}/\hbar^2, \tag{3}$$

$$\hat{T}_{00}^{(3)} = \left[[j_1 \otimes j_1]_2 \otimes [j_2 \otimes j_2]_2\right]_{00}/\hbar^4, \tag{4}$$

three anisotropic rank-2 tensors

$$\hat{T}_{2q}^{(1)} = [j_1 \otimes j_1]_{2q}/\hbar^2 + [j_2 \otimes j_2]_{2q}/\hbar^2, \tag{5}$$

$$\hat{T}_{2q}^{(2)} = [j_1 \otimes j_2]_{2q}/\hbar^2, \tag{6}$$

$$\hat{T}_{2q}^{(3)} = \left[[j_1 \otimes j_1]_2 \otimes [j_2 \otimes j_2]_2\right]_{2q}/\hbar^4, \tag{7}$$

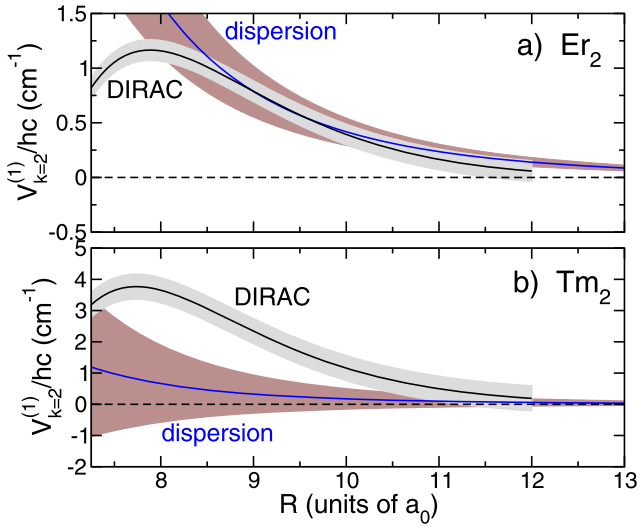

Figure 3. The fitted anisotropic spin-tensor strength $V^{(1)}_{k=2}(R)$ for Er_2 (panel a) and Tm_2 (panel b) as a function of R (black curve labeled DIRAC with gray one-standard-deviation uncertainty band). The strength is compared to the van-der-Waals dispersion potential $C^{(1)}_{k=2}/R^6$ (blue curve with brown one-standard-deviation uncertainty band).

and a single anisotropic rank-4 tensor

$$\hat{T}^{(1)}_{4q} = \left[[j_1 \otimes j_1]_2 \otimes [j_2 \otimes j_2]_2\right]_{4q}/\hbar^4. \tag{8}$$

Thus $N_0 = 3$, $N_2 = 3$, and $N_4 = 1$ in equation (1). We have followed the $\otimes$ notation of reference [31] for combining spherical tensor operators, which is equivalent to the notation used in reference [32]. Then I is the identity operator, and $[j_1 \otimes j_2]_{kq}$ denotes a tensor product of angular momentum operators $\vec{j}_1$ and $\vec{j}_2$ coupled to an operator of rank k and component q. Finally, $V^{(i)}_k(R)$ are R-dependent strengths with units of energy.

The eigenvalues of the interaction operator $V(\vec{\mathbf{R}})$ as functions of R correspond to the adiabatic electronic potentials. The corresponding eigenstates are R-dependent superpositions of $|j_1\Omega_1\rangle|j_2\Omega_2\rangle + \epsilon\sigma|j_2\Omega_2\rangle|j_1\Omega_1\rangle$ (excluding normalization) with the constraints that $\Omega = \Omega_1 + \Omega_2 \geqslant 0$ and *gerade/ungerade* inversion symmetry are conserved. Here, $\sigma = +1/-1$ for *gerade/ungerade* states and $\epsilon = +1/-1$ for Er and Tm, respectively.

We obtain the strengths $V^{(i)}_k(R)$ by a least-squares procedure minimizing the differences of the splittings with respect to the spin-stretched potential. We only do so for separations $R \leqslant 12a_0$ for which DIRAC 2019 converged. All $V^{(i)}_k(R)$ except $V^{(1)}_{k=0}(R)$ and $V^{(1)}_{k=2}(R)$ are consistent with zero. Thus, the dominant spin-tensor operators are either spin independent or a rank-2 tensor operator, corresponding to an R-dependent effective atomic quadrupole moment coupled to the rotation of the dimer. The spin-independent strength $V^{(1)}_{k=0}(R)$ closely follows the spin-stretch potential shown in figure 1. See the appendices for our recommended choice to construct the seven $V^{(i)}_k(R)$, for uncertainty budgets, and for the procedure to construct strengths for $R > 12a_0$.

The fitted $V^{(1)}_{k=2}(R)$ for Er_2 and Tm_2 are shown in figure 3 as functions of R up to $12a_0$. The anisotropic strength is positive, is at most a few times $hc \times 1\ \mathrm{cm}^{-1}$, and approaches zero for large R. Finally, these anisotropic strengths are at least two orders of magnitude smaller than $V^{(1)}_{k=0}(R)$. Tables with values for $V^{(1)}_{k=0}(R)$ and $V^{(1)}_{k=2}(R)$ can be found in the appendices.

The dominance of the isotropic spin-independent tensor operator is a consequence of the fact that the spatial extent of the 4f orbital is much smaller than that of the 6s orbital. In fact, the 4f orbital of one atom does not significantly overlap with that of a nearby Er or Tm atom even for R near the equilibrium separation.

We can now explain the origin of the patterns seen in figure 2. Including only the two dominant spin tensor operators in $V(\vec{\mathbf{R}})$, eigenstates of $V(\vec{\mathbf{R}})$ correspond to *single* $|j_1\Omega_1\rangle|j_2\Omega_2\rangle + \epsilon\sigma|j_2\Omega_2\rangle|j_1\Omega_1\rangle$ states. They have eigenenergies

$$V(R;\Omega) = V^{(1)}_{k=0}(R) + V^{(1)}_{k=2}(R)\frac{3(\Omega_1^2+\Omega_2^2) - 2j(j+1)}{\sqrt{6}}. \tag{9}$$

with quadratic or parabolic dependences on Ω_1 and Ω_2 (and thus Ω). For Er_2 with positive $V^{(1)}_{k=2}(R)$ and integer j, equation (9) predicts that the $\Omega_1 = \Omega_2 = 0$ state and thus an $\Omega = 0$ state has the lowest potential energy. In fact, for Er_2 this is a 0^+_g state. In addition, equation (9) implies that the energetically-highest $\Omega = 0$ state is degenerate with the sole spin-stretched $\Omega = 12$ state. In fact, multiple degenerate adiabatic states with the same value for Ω_1 but opposite-signed values for Ω_2 exist.

For Tm_2 also with positive $V^{(1)}_{k=2}(R)$ but now half-integer j, the model is quite satisfactory as well. Equation (9) predicts that states with $|\Omega_1| = |\Omega_2| = 1/2$ have the lowest energy. In this case, Ω_σ is either 0^+_g or 0^-_u (both with $\Omega_1 = -\Omega_2 = 1/2$) or 1_u (with $\Omega_1 = \Omega_2 = 1/2$) and the ground state should be three-fold degenerate. In fact, the energetically-lowest level from the DIRAC calculations is a 0^+_g state. Any removal of degeneracies is due to one or more of the five weaker spin-tensor operators not accounted for in equation (9).

Although the five weaker spin-tensor operators could not be reliably extracted from the least-squares adjustment to *all* splittings among the relativistic potentials of Tm_2, additional analyses show that the spin-tensors in equations (3) and (6) are the most important of the five. The first-order correction to the energy due to these two spin-tensor operators is

$$\left(-\frac{1}{\sqrt{3}}V^{(2)}_0(R) + \frac{2}{\sqrt{6}}V^{(2)}_2(R)\right)\Omega_1\Omega_2 \tag{10}$$

with a positive value within the parenthesis. Thus the 0^+_g state has a lower potential energy than the 1_u state.

2.3. Spin-tensors for long-range interactions

The results shown in figures 2 and 3 were focused on the deepest parts of the potentials. For scattering of ultracold atoms the long-range or large R part of the potential is equally important. The long-range form involves the van-der-Waals as well as magnetic and quadrupolar interactions.

In our model for $V(\vec{\mathbf{R}})$ all seven strengths $V^{(i)}_k(R)$ have a $C^{(i)}_k/R^6$ contribution for $R \to \infty$. Here, $C^{(i)}_k$ are van-der-Waals coefficients. The $k = 2, i = 2$ strength has a second long-range contribution. That is, $V^{(2)}_2(R) \to D^{(2)}_2/R^3 + C^{(2)}_2/R^6$, where $D^{(2)}_2/R^3$ describes the magnetic dipole–dipole interaction between the magnetic moments of the lanthanides atoms. Its strength $D^{(2)}_2$ is $-\sqrt{6}\alpha^2(g_j/2)^2E_\mathrm{h}a_0^3$, where g_j is the electronic g-factor of the atomic ground state, α is the fine-structure constant, and $E_\mathrm{h} = 4.359\,74 \times 10^{-18}$ J is the Hartree energy. The magnetic dipole-dipole interaction is not captured by electronic structure calculations, but is relevant for scattering calculations.

The rank-4 strength $V^{(1)}_{k=4}(R)$ has a second long-range contribution as well. It approaches $Q^{(1)}_4/R^5 + C^{(1)}_4/R^6$ for large R with a $1/R^5$ quadrupole–quadrupole term with coefficient $Q^{(1)}_4 = 6\sqrt{70}(\mathcal{Q}/ea_0^2)^2/[j_i^2(2j_i-1)^2] \times E_\mathrm{h}a_0^5$ for homonuclear dimers that is solely determined by the atomic quadrupole moment $\mathcal{Q} = \langle j_i j_i|Q_{20}|j_i j_i\rangle$ of the $m_i = j_i$ spin-stretched state of Er or Tm [33] and e is the positive elementary charge. The quadrupole moment for erbium was calculated in our previous paper [12] and equals $0.029ea_0^2$. For thulium $\mathcal{Q}$ is not available, but expected to be equally small compared to ea_0^2. For ro-vibrational simulations with thulium we use $\mathcal{Q} = 0$.

We have determined the $C^{(i)}_k$ coefficients for Er_2 and Tm_2 from second-order perturbation theory in the electric dipole-dipole interaction using experimentally-determined atomic transition frequencies and oscillator strengths or Einstein A coefficients as well as their reported uncertainties. We closely follow the calculations in references [10, 34] for the dysprosium dimer. The evaluation of the seven van-der-Waals coefficients is described in the appendices. Values are given in table 1, while correlation coefficients are given in the appendices. The relative sizes of the $C^{(i)}_k$ reinforce the observations regarding the strengths $V^{(i)}_k(R)$ derived from the electronic structure calculations

For Er_2 we observe that the absolute value of the magnetic dipole–dipole interaction $|D^{(2)}_2|/R^3$ equals $C^{(1)}_2/R^6$ at $R \approx 35a_0$ and $C^{(2)}_2/R^6$ at $R \approx 18a_0$. Hence, for $R \gg 35a_0$ the magnetic dipole–dipole interaction is the strongest anisotropic interaction, while for smaller R the effective quadrupole interaction of equation (5) is the strongest anisotropic interaction.

Less obvious from table 1 is that we have been able to derive non-trivial algebraic relationships among the $C^{(i)}_k$ thereby reducing the number of independent dispersion coefficients from 7 to 4. We find that

$$C^{(2)}_2 = \sqrt{2}C^{(2)}_0 \tag{11}$$

showing that the spin-exchange strength and the effective dipole–dipole strength multiplying equations (3) and (6), respectively, are related. Similarly, we find that

$$C^{(3)}_2 = \sqrt{\frac{10}{7}}C^{(3)}_0 \quad \text{and} \quad C^{(1)}_4 = 6\sqrt{\frac{18}{7}}C^{(3)}_0 \tag{12}$$

Table 1. Isotropic and anisotropic van-der-Waals dispersion coefficients $C_k^{(i)}$ for Er + Er and Tm + Tm sorted by value and then by rank k. The first three columns label the seven tensor operators. The last two columns give their value and its one-standard-deviation statistical uncertainties. The strength of tensor operator $[j_1 \otimes j_2]_2$ is $\sqrt{2}$ times larger than that of $[j_1 \otimes j_2]_0$. Similarly, the strengths of the last three tensor operators of each dimer are related by simple algebraic factors discussed in the text. For numerical convenience the strengths are given with additional digits.

Homonuclear erbium dimer				
k	i	Operator $T_k^{(i)}$	$C_k^{(i)}$ (units of $E_h a_0^6$)	$u(C_k^{(i)})$ (units of $E_h a_0^6$)
0	1	I	−1723.072 389 927	65
2	1	$[j_1 \otimes j_1]_2 + [j_2 \otimes j_2]_2$	1.903 660 883	0.57
0	2	$[j_1 \otimes j_2]_0$	0.171 750 953	0.099
2	2	$[j_1 \otimes j_2]_2$	0.242 892 527	0.14
0	3	$[[j_1 \otimes j_1]_2 \otimes [j_2 \otimes j_2]_2]_0$	−0.000 943 784	0.000 55
2	3	$[[j_1 \otimes j_1]_2 \otimes [j_2 \otimes j_2]_2]_2$	−0.001 128 037	0.000 66
4	1	$[[j_1 \otimes j_1]_2 \otimes [j_2 \otimes j_2]_2]_4$	−0.009 080 527	0.0053
Homonuclear thulium dimer				
0	1	I	−1672.115 030 649	54
2	1	$[j_1 \otimes j_1]_2 + [j_2 \otimes j_2]_2$	0.788 488 761	1.47
0	2	$[j_1 \otimes j_2]_0$	0.001 566 976	0.012
2	2	$[j_1 \otimes j_2]_2$	0.002 216 039	0.017
0	3	$[[j_1 \otimes j_1]_2 \otimes [j_2 \otimes j_2]_2]_0$	−0.000 309 025	0.000 60
2	3	$[[j_1 \otimes j_1]_2 \otimes [j_2 \otimes j_2]_2]_2$	−0.000 369 355	0.000 72
4	1	$[[j_1 \otimes j_1]_2 \otimes [j_2 \otimes j_2]_2]_4$	−0.002 973 250	0.0058

relating the strengths of the three spin-tensors constructed from the two effective atomic quadrupole operators $[j_1 \otimes j_1]_2$ and $[j_2 \otimes j_2]_2$. The derivation of these relations can be found in the appendices.

2.4. Ro-vibrational eigenstates

We finish our analyses of Er_2 and Tm_2 by computing their energetically-lowest ro-vibrational eigenstates. That is, we compute eigenstates of $-\hbar^2\nabla^2/(2\mu) + V(\vec{\mathbf{R}})$, where $\mu = m/2$ and m is the mass of the Er or Tm atom [35]. We discretize the radial component of the kinetic energy operator $-\hbar^2\nabla^2/(2\mu)$ using the discrete-variable representation of reference [36]. Details regarding the selection of the spin and angular momentum basis and, in particular, the orbital or partial-wave angular momentum $\vec{\ell}$ and total molecular angular momentum $\vec{J}$ of the two rotating atoms are given in section 3.3. We present results from two calculations. One is based on potential $V(\vec{\mathbf{R}})$ including only the two dominant spin tensors $\hat{T}_0^{(1)}$ and $\hat{T}_2^{(1)}$, constructed by joining the electronic structure data with the long-range potentials, and one where all seven tensor operators are included. For latter case, the R-dependence of the remaining five weaker spin tensor operators is given by their long-range form for all R.

Figure 4 shows three views of ro-vibrational eigenenergies of bosonic $^{168}Er_2$ states near the minimum of the adiabatic potentials. As the nuclear spin of ^{168}Er is zero *gerade* basis states have even values for partial wave ℓ. *Ungerade* basis states require odd ℓ. The pattern of the energy levels in the $hc \times 150$ cm^{-1} energy range in figure 4(a) can be understood from the seven 0_g^+ adiabatic potentials shown in figures 2(a) and (b) and equation (9). The vibrational energy spacing based on the harmonic approximation around the minima of the nearly-parallel adiabatic potentials is $hc \times 27.0$ cm^{-1} so that vibrational levels $v = 0, 1, \ldots, 5$ are visible in the figure. For each v the spacings among the seven 0_g^+ states are to good approximation found from $\sqrt{6}V_{k=2}^{(1)}(R_e)\Omega_1^2$ for $|\Omega_1| = 0, \ldots, 6$ with $\sqrt{6}V_{k=2}^{(1)}(R_e) = hc \times 2.3$ cm^{-1} at the equilibrium separation. The molecular fine-structure thus overlaps with the vibrational structure.

Figure 4(b) shows $v = 0$ $\Omega_{g/u}^{\pm}$ $^{168}Er_2$ eigenstates over an energy region of only $hc \times 15$ cm^{-1} versus total molecular angular momentum J. Based on calculations that include all spin tensors. Panel (c) shows equivalent data including only the two strongest spin tensors. The level density in both two panels is large, although the level patterns are distinct with differences around $hc \times 1$ cm^{-1}. In other words, the weaker spin-tensors cannot be ignored in an accurate analysis of the lowest energy states of Er_2.

Surprisingly, we predict that the $J = 10$ rotational state of the $v = 0$ 0_g^+ ground state has the absolute lowest energy when all interactions are included. The reason for this and other unexpected rotational progressions is the degeneracies of different Ω states inherent in the model of equation (9) as well as more accidental degeneracies due to the high level density. The Coriolis force in a rotating molecule breaks these (near-)degeneracies for states with Ω values that differ by one unit. For large J coupling matrix elements are on the order of $B_e J j_1$, which can easily reach values of order $hc \times 1$ cm^{-1} comparable to or larger than $V_{k=2}^{(1)}(R_e)$, even when B_e is not. Degenerate perturbation theory then predicts 'rotational' progressions

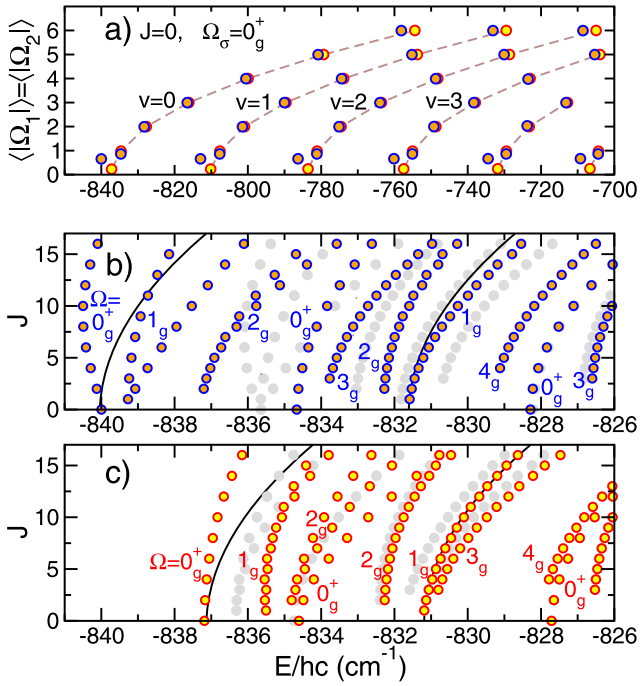

Figure 4. Three views of eigenenergies E of bosonic $^{168}Er_2$ near the minima of its potentials. Energies are with respect to the dissociation limit of two ^{168}Er atoms. Panel (a) shows the energies of the fine-structure components for the six energetically-lowest $J = 0$ vibrational levels v of the 0_g^+ state. For each v these 0_g^+ states are uniquely labeled by the expectation value of $|\Omega_1|$, which are close to integer valued. Orange-filled and yellow-filled circles are the result of calculations that include all spin-tensor interactions and only include the two strongest spin tensors, respectively. Panel (b) shows the energies of $v = 0$ rotational eigenstates versus J for calculations that include all tensor operators, while panel (c) shows equivalent data including only the two strongest spin tensors. Labeled colored circles correspond to *gerade* states. Solid gray markers correspond to the energies of *ungerade* states. Finally, black curves in panels (b) and (c) correspond to progressions $B_eJ(J+1)$, where $B_e = hc \times 0.0095$ cm^{-1} is the rotational constant at the equilibrium separation. Note the different energy range in panel (a) versus that in panels (b) and (c).

of the form $\pm A_eJ + B_eJ(J+1)$, where energy A_e with $|A_e| \gg B_e$ can be computed on a case by case basis.

Figure 5 shows the lowest eigenenergies of $^{169}Tm_2$ near the minimum of its adiabatic potentials versus total molecular angular momentum J. Both *gerade* and *ungerade* states are shown and assigned $\Omega_{g/u}^{\pm}$ labels. The nuclear spin $\vec{\imath}$ of ^{169}Tm is 1/2, making the atoms bosons, and hyperfine interactions of the form $a_{\rm hf}\vec{\jmath}_1 \cdot \vec{\imath}_1/\hbar^2$ etc mix *gerade* and *ungerade* states, although even and odd ℓ remain uncoupled. We do not include such interactions and *gerade* states with either even and odd ℓ must be shown. Similarly, *ungerade* states with even and odd ℓ exist. It is worth noting that the ^{169}Tm hyperfine constant $a_{\rm hf} = hc \times 0.0062$ cm^{-1} [16] and hyperfine couplings can mostly be neglected in the analysis of the bound states on the scale shown in the figure.

The Tm_2 level structure is significantly simpler than that for Er_2, even though the vibrational spacings and rotational constants of the two dimers are nearly the same. The dominant anisotropic spin-tensor interaction in Tm_2 is close to three times larger than in Er_2, as seen in figure 3, thereby reducing the number of $\Omega_\sigma^{\pm}$ states between the $v = 0$ and 1 vibrational states. The vibrational and rotational spectroscopic constants for Tm_2 are $hc \times 27.2$ cm^{-1} and $hc \times 0.0096$ cm^{-1}, respectively. Unlike for Er_2 the remaining five weaker spin-tensor operator play no significant role.

Figure 5(b) shows that the $v = 0$, $J = 0$ 0_g^+ state is the absolute ground state. This 0_g^+ state has a 'simple' $B_eJ(J+1)$ rotational progression. The nearby *ungerade* states have a less-conventional rotational progression. Here, this follows from the *four*-fold degeneracy for the lowest-energy states implied by equation (9). The four states have $|\Omega_1| = |\Omega_2| = 1/2$ and labels $\Omega_\sigma^{\pm} = 0_g^+, 0_u^-$ and twice 1_u. In fact, a careful analytical analysis of the centrifugal and coriolis interactions within the degenerate manifold shows that in the limit $J \to 0$ the *ungerade* levels have energies that lie tens of B_e above that of the 0_g^+ state. For large J two of the three *ungerade* states become equal mixtures of 1_u and 0_u^-. The *ungerade* state with the second-lowest energy remains of pure 1_u symmetry. Finally, we observe that the energetically-lowest *ungerade* state has $J = 3$.

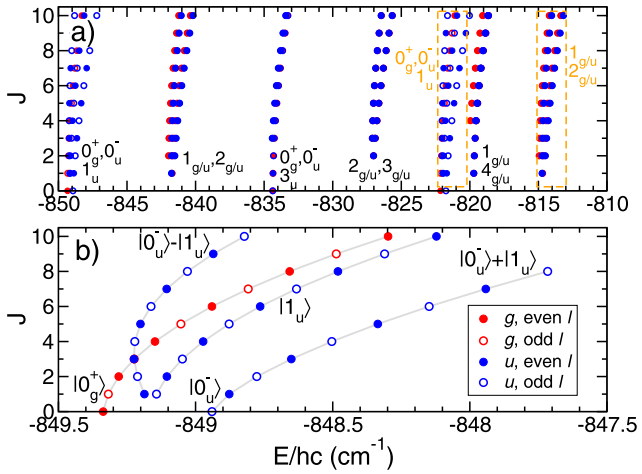

Figure 5. Eigenenergies E of $^{169}Tm_2$ near the minima of its potentials. Energies are with respect to the dissociation limit of two ^{169}Tm atoms. Panel (a) shows energies of $v = 0$ and $v = 1$ $\Omega_\sigma^\pm$ vibrational and fine-structure eigenstates versus total molecular angular momentum J for calculations that include all spin-tensors interactions. Levels enclosed by orange dashed boxes are $v = 1$ states. All others are $v = 0$ states. Panel (b) shows a blowup of the energies of the energetically-lowest 0_g^+, 0_u^-, and 1_u states. Unusual rotational progressions are visible and are discussed in the text. Color and type of markers, as indicated in the legend box, separate *gerade* from *ungerade* states as well as even from odd partial wave ℓ states and are the same in both panels. Note the different energy ranges shown in the two panels.

3. Methods

3.1. Spin-stretched electronic potentials

The spin-stretched potentials $V_{ss}(R)$ for Er_2 and Tm_2 have been obtained from (partially-) spin-restricted single-reference non-relativistic coupled-cluster calculations that included single, double and perturbative triple (RCCSD(T)) excitations [37]. For the calculations the total electron spin S is 2 and 1 for Er_2 and Tm_2, respectively. In addition, the projection quantum number Λ of the total electron orbital angular momentum along the internuclear axis is 10 and 6 for Er_2 and Tm_2, respectively.

We use the Stuttgart/Cologne 'small-core' quasi-relativistic effective core potentials (ECPs) developed for rare-earth elements (ECP28MWBSO) [38] to describe the twenty eight 1s, 2sp, and 3spd electrons of the Er and Tm atoms. The remaining electrons are described by the relativistic small core segmented [39] atomic basis set of quadruple-zeta quality developed for the ECPs. We extend the basis set with three diffuse Gaussian s functions with exponents 0.1495, 0.01, and 0.004 12; two p functions with exponents 0.048 95 and 0.0211; one d function with exponent 0.027 99; and one f and g function both with exponent 0.1068, respectively. All exponents are in units of a_0^{-2}. In order to converge the preliminary self-consistent-field (SCF) calculations of neutral Er_2 and Tm_2, we start from the SCF orbitals for molecular ions Er_2^{4+} and Tm_2^{4+}.

Based on a comparison of results found with different basis set size, the one-standard-deviation uncertainty of the spin-stretched potential is about $hc \times 50$ cm^{-1} at the equilibrium separation and drops to less than $hc \times 1$ cm^{-1} at $R = 20a_0$. See tables in the appendices for precise data on the spin-stretched potentials. A description of the extrapolation to $R > 20a_0$ can also be found there.

3.2. Relativistic calculation of potential splittings

We use the direct relativistic configuration interaction (DIRRCI) method [40] in DIRAC [29] to determine the energy splittings between the relativistic adiabatic potential curves of Er_2 and Tm_2 dissociating to two ground-state atoms.

As in the non-relativistic calculations converging SCF calculations for the neutral dimers start from SCF orbitals for Er_2^{4+} and Tm_2^{4+}. A reordering of the occupied 6s and open-shell 4f orbitals is then required in the input data for DIRAC. In practice, we only determine the SCF orbitals at $R = 12a_0$ in this manner. SCF orbitals for $R < 12a_0$ are found starting from orbitals for the neutral dimer obtained for a slightly larger R. We repeat the scheme to small R until the potentials are repulsive.

The active space in the DIRRCI calculations is solely composed of molecular orbitals arising from the 4f atomic shells. The 6s orbitals are kept doubly occupied and are not part of the active space. In addition, 5d orbitals remain unoccupied. These constraints balance the need for reasonable estimates of splittings among the relativistic potentials and a reasonable run-time and memory usage for the calculations. For $R > 12a_0$, we find that the splittings contain noticeable numerical noise and unphysical jumps, sometimes reordering

states. This is likely due to an insufficient accuracy of molecular orbitals in the initial SCF calculations. We do not include $R > 12a_0$ DIRAC calculations in our analysis. For state assignment it proved useful to determine the expectation values of the z-components of the total electronic orbital angular momentum and spin operators along the internuclear axis.

DIRRCI calculations have been performed for 25 and 28 internuclear separations between $7a_0 < R \leqslant 12a_0$ for Er_2 and Tm_2, respectively. At each of these R values, we determine the 91 relativistic potential energies and eigenstates for Er_2. For Tm_2 we find 36 eigenpairs. An eigenstate is uniquely labeled by $n, \Omega^{\pm}_{g/u}$ with $n = 1, 2, 3, \ldots$ for $\Omega^{\pm}_{g/u}$ states ordered by increasing potential energy. We denote relativistic eigenenergies by $U_{\rm rel}(R; n, \Omega^{\pm}_{g/u})$. For the 12_g and 7_u spin-stretched state for Er_2 and Tm_2, respectively, there exists just one potential dissociating to two ground state atoms. For our identical ground-state atoms *gerade* states are 0^+ states, while *ungerade* states are 0^- states. A discussion of di-atomic symmetries and molecular state labels can be found in references [41, 42].

With the constraints on the active space in the DIRRCI calculations, we sacrificed on the accuracy of the depth of the potentials. Those are mainly determined by excitations of electrons out of the 6s orbitals. In order to obtain accurate adiabatic potential energy curves $V_{\rm rel}(R; n, \Omega^{\pm}_{g/u})$, we assume that the non-relativistic spin-stretched potential $V_{\rm ss}(R)$ is a good representation of the potential for the relativistic spin-stretched state. The adiabatic potentials for the other adiabatic states are then

$$V_{\rm rel}(R; n, \Omega^{\pm}_{g/u}) = V_{\rm ss}(R) - \left(U_{\rm rel}(R; n, \Omega^{\pm}_{g/u}) - U_{\rm rel}(R; 1, \Omega_{\rm ss})\right) \tag{13}$$

when $R \leqslant 12a_0$ and $\Omega_{\rm ss} = 12_g$ and 7_u for Er_2 and Tm_2, respectively. The uncertainties in the $R \leqslant 12a_0$ calculations and extrapolation to $R > 12a_0$ using the long-range dispersion potentials are discussed in the appendices. The potentials in equation (13) are used in the least-squares fitting to spin-tensor operators as described in the main text.

3.3. Basis sets in ro-vibrational state calculations

We use the unit-normalized coupled spin and angular momentum basis

$$|(j_{\rm el}\ell)JM\rangle \equiv \sum_{m_j m_\ell} |(j_1 j_2) j_{\rm el} m_{\rm el}\rangle Y_{\ell m_\ell}(\hat{\mathbf{R}}) \langle j_{\rm el}\ell m_{\rm el} m_\ell | JM\rangle \tag{14}$$

for the calculation of ro-vibrational states of Er_2 and Tm_2 with

$$|(j_1 j_2) j_{\rm el} m_{\rm el}\rangle = \sum_{m_1 m_2} |j_1 m_1\rangle |j_2 m_2\rangle \langle j_1 j_2 m_1 m_2 | j_{\rm el} m_{\rm el}\rangle$$

and spherical harmonic functions $Y_{\ell m}(\hat{\mathbf{R}})$. Here, $\langle j_1 j_2 m_1 m_2 | jm\rangle$ are Clebsch–Gordan coefficients. The total molecular angular momentum $\vec{J} = \vec{\ell} + \vec{j}_{\rm el}$ is conserved, $\vec{j}_{\rm el} = \vec{j}_1 + \vec{j}_2$, and projection quantum numbers m_x and M are with respect to a space-fixed coordinate system. Basis states with even and odd $j_{\rm el}$ contribute to *gerade* and *ungerade* molecular states, respectively, and are not mixed by the molecular Hamiltonian. Similarly, the Hamiltonian does not couple basis states with even partial wave ℓ with those with odd ℓ. Atomic masses have been taken from references [43, 44] and atomic g-factors from reference [45].

4. Conclusions

We have studied the electronic properties of two heavy homonuclear lanthanide molecules, Er_2 and Tm_2. A hybrid non-relativistic/relativistic electronic structure approach was needed to overcome the computational challenges arising from the complexity of their open submerged 4f electronic shell structure partially hidden by a closed $6s^2$ shell. This allowed us for the first time to determine a complete set of ground-state potentials for a wide range of interatomic separations.

A non-relativistic coupled-cluster calculation was used to determine the spin-stretched PESs with the maximum allowed total electron spin S and projection quantum number Λ of the total electron orbital angular momentum along the internuclear axis. Then we used a relativistic multi-configuration-interaction calculation to determine the splittings among the potentials dissociating to two ground state atoms. There are 91 *gerade/ungerade* potentials for Er_2 (with Ωs from 0 to 12) and 36 potentials for Tm_2 (with Ωs from 0 to 7). We identified the splittings as due to different relative orientations of the angular momenta of 4f shell electrons.

To facilitate the application of our electronic structure predictions in spectroscopic and scattering dynamics studies we analytically expressed the potential energy operator for Er_2 and Tm_2 as a sum of a small number of spherical-tensor operators and elucidated the relationships between their electrostatic,

relativistic, and magnetic dipole–dipole interactions. The largest tensor operator is spin-independent and isotropic, followed by an anisotropic one coupling the quadrupole moment of the atom to the rotation of the molecule.

Finally, we computed the spectroscopically relevant lowest ro-vibrational eigenstates of Er_2 and Tm_2. This data can be used as preliminary information for setting up spectroscopic studies of these exotic and technologically important systems.

Acknowledgments

Work at Temple University is supported by the US Air Force Office of Scientific Research Grant #FA9550-21-1-0153, the Army Research Office Grant #W911NF-17-1-0563, and the NSF Grant #PHY-1908634.

Data availability statement

All data that support the findings of this study are included within the article (and any supplementary files).

Appendix A. Table of content for appendices

These appendices contain the input data and a derivation needed to reproduce the potentials presented in our article on the interactions between two ground-state erbium atoms and two ground-state thulium atoms. We give tables for non-relativistic spin-stretched potentials and relativistic anisotropic spin-tensor strengths. The main text has a graph of the potentials of *gerade* states of the two dimers. Here, we present the equivalent figure of potentials for *ungerade* states.

In addition, we derive the long-range van-der-Waals dispersion interactions for our high-spin Er and Tm atoms. We find that these interactions can be described in terms of seven spin-tensor operators, whose strengths or van-der-Waals coefficients are linearly dependent. In fact, only four independent dispersion coefficients exist. We also give tables of Er and Tm atomic transition frequencies and Einstein A coefficients or oscillator strengths on which the values of the dispersion coefficients in the table in the main text are based.

We use Planck's constant h and the speed of light in vacuum c in converting energies into wavenumbers.

Appendix B. Non-relativistic spin-stretched states of Er_2 and Tm_2

The spin-stretched potentials for Er_2 and Tm_2 dissociating to two ground-state atoms have been obtained from non-relativistic single-reference coupled-cluster calculations that included single, double and perturbative triple excitations (RCCSD(T)). The orbital basis sets for these calculations have been described in section 3. The total electron spin S and orbital-angular-momentum projection quantum number Λ are conserved quantities and for this state have their maximum allowed value. We have $(S, \Lambda) = (2, 10)$ and $(1, 6)$ for Er_2 and Tm_2, respectively.

The spin-stretched potential $U_{ss}(R)$ for Er_2 has been determined with coupled-cluster theory as implemented in CFOUR [46] at 59 separations between $R_{min} = 7.3a_0$ and $R_{max} = 20a_0$ as well as at $R_\infty = 200a_0$ in order to determine the dissociation energy of the potential. Here, $a_0 = 0.052\,9177$ nm is the Bohr radius. The spin-stretched potential for Tm_2 has been determined using coupled-cluster theory as implemented in Molpro [47] at 72 separations between $R_{min} = 6.25a_0$ and $R_{max} = 20a_0$ as well as at $R_\infty = 60a_0$. Potentials

$$V_{ss}(R) = U_{ss}(R) - U_{ss}(R_\infty) \tag{B1}$$

of Er_2 and Tm_2 up to $R = R_{max}$ are given in tables 2 and 3, respectively.

The spin-stretched potential for $R < R_{min}$ is found by linear extrapolation using the first two separations larger than or equal to R_{min}. For $R > R_{disp}$ with $R_{disp} > R_{max}$ we use the dispersive form

$$V_{disp}(R) = C_{6,ss}/R^6 + C_{8,ss}/R^8 + C_{10,ss}/R^{10}, \tag{B2}$$

where the van-der-Waals coefficient $C_{6,ss}$ is

$$C_{ss} = C_0^{(1)} + (2j)(2j-1)C_2^{(1)}/\sqrt{6} \tag{B3}$$

with $j = 6$ and 7/2 for Er_2 and Tm_2, respectively based on two relevant values for $C_k^{(i)}$ are given in the table in the main text and the derivation in this appendix B. Coefficients $C_{8,ss}$ and $C_{10,ss}$ are fixed such that the

Table 2. Potential energy $V_{ss}(R)$ of the energetically-lowest 'spin-stretched' state of $Er_2\,\Omega = 12_g$ as function of internuclear separation R. The R-dependent uncertainty of this potential is discussed in the text.

R/a_0	V_{ss}/hc (cm^{-1})	R/a_0	V_{ss}/hc (cm^{-1})	R/a_0	V_{ss}/hc (cm^{-1})
7.3	136.928 967 055 564	9.3	−702.972 094 884 141	11.6	−290.170 412 396 272
7.4	−33.406 301 542 6345	9.4	−685.377 674 371 753	11.8	−265.152 758 759 965
7.5	−179.030 466 142 739	9.5	−666.764 780 470 275	12.2	−221.189 686 201 221
7.6	−302.624 146 371 783	9.6	−647.392 883 509 601	12.6	−184.510 652 309 416
7.7	−406.626 745 855 377	9.7	−627.480 644 193 817	13.0	−154.076 250 986 245
7.8	−493.261 808 207 445	9.8	−607.236 006 360 562	13.5	−123.313 365 467 909
7.9	−564.543 330 776 862	9.9	−586.808 634 364 519	14.0	−99.051 708 898 4615
8.0	−622.296 924 164 693	10.0	−566.344 786 996 666	14.5	−79.886 802 233 5593
8.1	−668.163 414 255 055	10.1	−545.963 873 169 331	15.0	−64.705 663 449 5449
8.2	−703.629 551 622 843	10.2	−525.767 267 986 650	15.5	−52.640 114 033 3373
8.3	−730.026 393 137 440	10.3	−505.840 657 675 087	16.0	−43.017 485 089 5937
8.4	−748.547 347 148 735	10.4	−486.253 895 514 174	16.5	−35.313 312 122 6139
8.5	−760.256 868 094 275	10.5	−467.064 631 313 888	17.0	−29.121 524 427 1569
8.6	−766.106 999 612 316	10.6	−448.319 777 407 923	17.5	−24.127 342 901 4569
8.7	−766.942 290 212 839	10.7	−430.056 805 726 134	18.0	−20.083 495 395 4821
8.8	−763.511 447 018 345	10.8	−412.304 806 381 708	18.5	−16.795 839 427 4081
8.9	−756.477 032 518 151	10.9	−395.085 506 635 547	19.0	−14.113 977 371 4497
9.0	−746.423 038 708 948	11.0	−378.414 408 279 889	19.5	−11.909 450 699 9236
9.1	−733.862 648 819 818	11.2	−346.752 289 713 281	20.0	−10.094 344 030 2398
9.2	−719.246 967 350 335	11.4	−317.346 954 936 712		

Table 3. Potential energy $V_{ss}(R)$ of the energetically-lowest 'spin-stretched' state of Tm_2 as function of internuclear separation R. The R-dependent uncertainty of this potential is discussed in the text.

R/a_0	V_{ss}/hc (cm^{-1})	R/a_0	V_{ss}/hc (cm^{-1})	R/a_0	V_{ss}/hc (cm^{-1})
6.25	3874.150 188 674 83	8.6	−775.049 924 968 957	10.75	−409.392 022 314 815
6.5	2452.881 954 497 37	8.7	−772.468 793 423 23	11.0	−367.345 465 164 348
6.75	1398.481 432 962 68	8.75	−769.709 228 982 994	11.25	−328.942 955 195 758
6.8	1224.595 206 433 07	8.8	−766.073 434 020 327	11.5	−294.175 889 173 847
6.9	909.168 531 269 16	8.9	−756.484 235 631 714	11.75	−262.878 651 327 859
7.0	633.431 409 261 034	9.0	−744.222 911 614 132	12.0	−234.883 475 377 653
7.1	393.453 268 965 899	9.1	−729.769 650 342 498	12.25	−209.924 884 847 286
7.2	185.614 885 631 341	9.2	−713.532 718 742 361	12.5	−187.720 788 736 913
7.25	92.684 339 502 4816	9.25	−704.864 106 741 569	12.75	−168.003 713 562 084
7.3	6.567 910 359 323 26	9.3	−695.884 191 964 824	13.0	−150.499 513 340 797
7.4	−146.706 530 584 091	9.4	−677.132 015 128 778	13.5	−121.195 083 284 982
7.5	−276.986 305 870 368	9.5	−657.551 518 907 663	14.0	−98.021 831 132 6522
7.6	−386.841 551 372 091	9.6	−637.379 384 988 748	14.5	−79.616 511 988 0272
7.7	−478.589 634 023 197	9.7	−616.821 173 105 488	15.0	−64.911 337 709 8249
7.75	−518.306 204 431 474	9.75	−606.453 871 377 68	15.5	−53.123 749 640 7613
7.8	−554.273 972 390 536	9.8	−596.054 548 248 776	16.0	−43.650 785 151 5064
7.9	−615.850 590 443 533	9.9	−575.229 126 068 204	16.5	−36.020 200 485 7629
8.0	−664.991 862 988 103	10.0	−554.467 856 276 277	17.0	−29.854 652 957 0767
8.1	−703.262 622 294 269	10.1	−533.883 746 459 349	17.5	−24.854 757 166 5504
8.2	−732.035 857 769 05	10.2	−513.570 051 395 331	18.0	−20.775 206 334 3089
8.25	−743.254 940 662 834	10.25	−503.537 338 666 485	18.5	−17.464 628 932 3737
8.3	−752.551 798 724 083	10.3	−493.597 463 728 117	19.0	−14.746 852 461 4891
8.4	−765.919 099 466 286	10.4	−474.031 826 052 711	19.5	−12.515 387 932 7555
8.5	−773.126 032 186 692	10.5	−454.926 141 284 319	20.0	−10.664 119 330 474

dispersive form agrees with the potential energy from coupled-cluster theory at the two largest radial points $R \leqslant R_{max}$. We use $R_{disp} = R_{max} + 0.5a_0$ for both Er_2 and Tm_2, add $(R_{disp}, V_{disp}(R_{disp}))$ to the coupled-cluster data, and for $R \in (R_{min}, R_{disp})$ interpolate this extended coupled-cluster data set times R^6 using the Akima spline [48]. The function $R^6 V_{ss}(R)$ varies significantly less than $V_{ss}(R)$. The fitted $C_{8,ss}$ are consistent with typical values based on the induced quadrupole-quadrupole interaction for other di-atomic molecules [49] and the contributions from the five omitted dispersion terms is small compared to the uncertainties in the potentials.

The uncertainty budget of $V_{ss}(R)$ as function of R has two components. The first is the complete basis set error of the RCCSD(T) calculations. The second is that four-electron excitations might need to be included in our open-shell molecules. This corresponds to accounting for non-perturbative triple as well as quadruple excitations. Basis-set superpositions errors increase the depth of the potentials $V_{ss}(R)$, while

non-perturbative triple and quadruple corrections often are of opposite sign, nearly cancel, but lead to shallower potentials for dimers [50, 51]. Here, based on the differences of calculations with triple- and quadruple-zeta accuracy basis sets, we assume that the one-standard-deviation uncertainties of $V_{ss}(R)$ is $2 \times u(C_0^{(1)})/R^6$ for $R < R_{max}$, where $u(C_0^{(1)})$ is the one-standard-deviation uncertainty of the isotropic dispersion coefficient $C_0^{(1)}$.

Appendix C. Relativistic configuration-interaction calculations and expansion in spin tensor operators

We have used the DIRRCI method in DIRAC 2019 [29] to determine the energy splittings among the relativistic adiabatic potential curves of Er_2 and Tm_2 for $R \leqslant 12a_0$. Basis sets have been described in section 3. In section 3, we also described how the spin-stretched potential $V_{ss}(R)$ and the energy splittings are used to construct relativistic adiabatic potential curves $V_{rel}(R; n, \Omega^{\pm}_{g/u})$. We find a common uncorrelated one-standard-deviation uncertainty $u(R) = hc \times 10\ \mathrm{cm}^{-1}$ independent of R for all potential energy splittings. This follows from a comparison of DIRRCI calculations with different basis set size. In addition, the uncertainty in the splittings and that of $V_{ss}(R)$ are uncorrelated.

The $V_{rel}(R; n, \Omega^{\pm}_{g/u})$ were fit to an expansion in terms of seven spin–spin tensor operators with strengths $V_k^{(i)}(R)$ defined in the main text. Only $V_0^{(1)}(R)$ and $V_2^{(1)}(R)$ were found to be statistically relevant and we finally decided to only present results with those two strengths as fitting parameters with the remaining five strengths set to zero. The reduced chi-square χ^2_ν of this adjustment is less than one for all $R < 12a_0$ so that the fit is consistent.

Tables 4 and 5 contain values of the spin tensor strengths $V_0^{(1)}(R)$ and $V_2^{(1)}(R)$ as functions of interatomic separations for Er_2 and Tm_2, respectively. Note that as the uncertainty in the splittings and that of $V_{ss}(R)$ are uncorrelated strictly speaking strength $V_2^{(1)}(R)$ is the only adjusted constant and

$$V_0^{(1)}(R) = V_{ss}(R) - (2j)(2j-1)V_2^{(1)}(R)/\sqrt{6}, \tag{C1}$$

where $j = 6$ and 7/2 for Er_2 and Tm_2, respectively. The spin-tensor strength $V_2^{(1)}(R)$ has an one-standard-deviation uncertainty of $hc \times 0.094\ \mathrm{cm}^{-1}$ and $hc \times 0.40\ \mathrm{cm}^{-1}$ for Er_2 and Tm_2 independent of R, respectively. The uncertainty of $V_0^{(1)}(R)$ follows from error propagation of equation (C1). The contribution from $V_{ss}(R)$ always dominates. In addition, the absolute value of the difference between $V_0^{(1)}(R)$ and $V_{ss}(R)$ are no larger than the uncertainty of $V_{ss}(R)$ for all R. Hence, we surmise that the relativistic corrections to the non-relativistic spin-stretched potential $V_{ss}(R)$ are of similar magnitude as well.

For $R > 12a_0$ the relativistic configuration-interaction calculations do not converge. As shown in figure 4 in the main text, however, the adjusted anisotropic strengths $V_2^{(1)}(R)$ at $R = 12a_0$ for the two dimers are already consistent, i.e. within our uncertainties, with its asymptotic van-der-Waals $C_2^{(1)}/R^6$ behavior. We then use the van-der-Waals behavior for $R > R_{rel}$ with $R_{rel} = 12a_0 + 0.5a_0$. A smooth connection of the strength between $12a_0$ and R_{rel} is ensured by adding point $(R_{rel}, C_2^{(1)}/R_{rel}^6)$ to the $R \leqslant 12a_0$ fitted values for $V_2^{(1)}(R)$ and interpolate $R^6 V_2^{(1)}(R)$ with the Akima spline [48].

Finally, even though the five weaker $V_k^{(i)}(R)$ are consistent with zero in the least-squares adjustment, we use $V_k^{(i)}(R) = C_k^{(i)}/R^6$ for all R for these five strengths in the calculation of the rovibrational levels of Er_2 and Tm_2.

Figure 6 shows the *ungerade* potentials of Er_2 and Tm_2 near their equilibrium separation. The figure complements the figure with *gerade* state potentials in the main text

Appendix D. Derivation of the dispersion potentials

Long-range van-der-Waals dispersion interactions have been derived and studied in many settings [34, 52–54]. We repeat part of these derivations in order to explain the relationships among the strengths of the seven spin-tensor operators contributing the atom-atom interaction $V(\vec{\mathbf{R}})$ for large separations R. In this section we rely on reference [32] for notation regarding angular momentum operators as well as the manipulation of these operators with one clearly-stated exception regarding reduced matrix elements.

We consider interacting atoms with electronic eigenstates $|nb\beta\rangle$ with total electronic angular momentum quantum numbers b, projection quantum numbers β on a space- or laboratory-fixed axis, and energies E_{nb} that are independent of β. Label n further uniquely specifies states. The ground state of the atoms is $|gjm\rangle$.

The van-der-Waals potential operator between two ground-state atoms, $|g_1 j_1 m_1, g_2 j_2 m_2\rangle = |g_1 j_1 m_1\rangle |g_2 j_2 m_2\rangle$, is derived from (degenerate) second-order perturbation theory in the anisotropic electric

Table 4. Spin tensor strengths $V_0^{(1)}(R)$ and $V_2^{(1)}(R)$ for Er_2 as functions of separation R for $R \leqslant 12a_0$. The isotropic strength $V_0^{(1)}(R)$ is found from equation (C1). Its R-dependent uncertainty equals that of the potential of the spin-stretched state. The uncertainty of $V_2^{(1)}(R)$ is $hc \times 0.094$ cm^{-1} independent of R.

R/a_0	$V_0^{(1)}/hc$ (cm^{-1})	$V_2^{(1)}/hc$ (cm^{-1})
7.2		0.753 349 48
7.4	−86.142 826 11	0.978 618 00
7.6	−362.331 598 84	1.107 975 70
7.8	−555.792 687 57	1.160 369 30
8.0	−684.701 380 46	1.158 023 30
8.2	−763.820 046 90	1.116 939 40
8.4	−805.155 666 99	1.050 465 90
8.6	−818.303 474 06	0.968 596 43
8.8	−810.885 319 12	0.879 104 65
9.0	−788.864 471 84	0.787 574 66
9.2	−756.857 582 80	0.697 930 43
9.4	−718.377 859 98	0.612 375 88
9.6	−676.095 385 48	0.532 624 88
9.8	−632.016 380 40	0.459 842 97
10.0	−587.592 963 66	0.394 296 90
10.2	−543.844 352 18	0.335 451 76
10.4	−501.521 231 95	0.283 312 00
10.6	−461.135 226 34	0.237 812 96
10.8	−423.001 435 47	0.198 494 57
11.0	−387.293 699 89	0.164 770 71
11.2	−354.080 269 01	0.135 983 41
11.4	−323.360 789 65	0.111 597 17
11.6	−295.070 537 24	0.090 930 34
11.8	−269.111 696 06	0.073 464 97
12.0		0.058 714 69

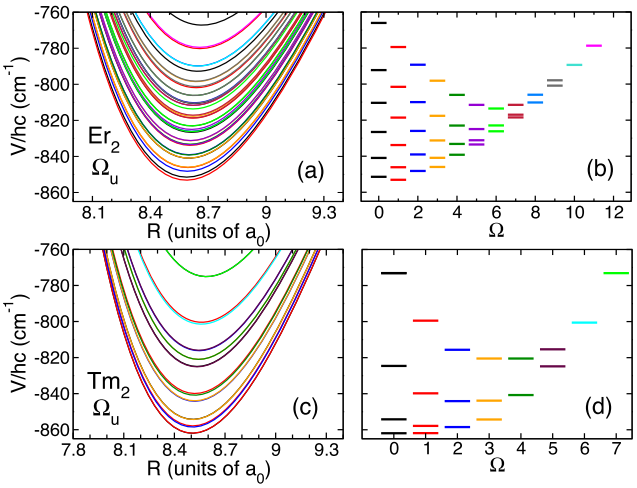

Figure 6. Relativistic $\Omega_u^{\pm}$ potential energy curves with *ungerade* symmetry for Er_2 (panel a) and Tm_2 (panel c) as functions of internuclear separation R near the equilibrium separation as obtained from electronic structure calculations. All potentials approach zero energy for $R \to \infty$. Panels (b) and (d) show potential energies from panels (a) and (c) using the same line colors at the equilibrium separation as functions of projection quantum number Ω for Er_2 and Tm_2, respectively. *Ungerade* $\Omega = 0$ states are 0^- states.

dipole-dipole interaction $V_{\rm dd}(\vec{\mathbf{R}})$ and is given by

$$V_{\rm vdW}(\vec{\mathbf{R}}) = \sum_{n_1 b_1 \beta_1,\ n_2 b_2 \beta_2}{}' V_{\rm dd}(\vec{\mathbf{R}})|n_1 b_1 \beta_1, n_2 b_2 \beta_2\rangle \frac{1}{E_{g_1 j_1} + E_{g_2 j_2} - E_{n_1 b_1} - E_{n_2 b_2}} \langle n_1 b_1 \beta_1, n_2 b_2 \beta_2 | V_{\rm dd}(\vec{\mathbf{R}}), \quad \text{(D1)}$$

where

$$V_{\rm dd}(\vec{\mathbf{R}}) = -\frac{1}{4\pi\epsilon_0}\sqrt{6}\frac{1}{R^3} T_2(d_1, d_2) \cdot C_2(\hat{\mathbf{R}}), \quad \text{(D2)}$$

d_i is the rank-1 electric dipole moment operator of atom $i = 1$ or 2, $C_{kq}(\hat{\mathbf{R}})$ is a spherical harmonic, and rank-k spherical-tensor operator $T_{kq}(R, S) \equiv [R \otimes S]_{kq}$ with the $\otimes$ notation of [31] is constructed from

Table 5. Spin tensor strengths $V_0^{(1)}(R)$ and $V_2^{(1)}(R)$ for Tm_2 as functions of separation R for $R \leqslant 12a_0$. The isotropic strength $V_0^{(1)}(R)$ is found from equation (C1). Its R-dependent uncertainty equals that of the potential of the spin-stretched state. The uncertainty of $V_2^{(1)}(R)$ is $hc \times 0.40\ \mathrm{cm}^{-1}$ independent of R.

R/a_0	$V_0^{(1)}/hc\ (\mathrm{cm}^{-1})$	$V_2^{(1)}/hc\ (\mathrm{cm}^{-1})$
7.0	594.906 552 04	2.246 8153
7.2	133.540 325 87	3.037 0500
7.4	−206.867 117 84	3.508 6367
7.6	−450.800 902 36	3.730 1851
7.8	−618.718 066 62	3.758 4559
8.0	−727.597 306 29	3.651 2236
8.1	−764.327 963 12	3.561 4030
8.2	−791.258 439 38	3.453 9311
8.3	−809.698 587 44	3.332 8684
8.4	−820.814 682 19	3.201 5754
8.5	−825.645 850 40	3.063 0180
8.6	−825.113 513 91	2.919 7678
8.7	−820.036 541 42	2.774 2074
8.8	−811.133 570 04	2.627 9605
8.9	−799.049 674 38	2.482 4668
9.0	−784.329 271 35	2.339 0504
9.1	−767.469 327 13	2.198 6898
9.2	−748.892 381 32	2.062 2174
9.3	−728.980 728 35	1.930 2292
9.4	−708.050 363 58	1.803 1947
9.5	−686.382 234 86	1.681 4415
9.6	−664.216 950 40	1.565 1986
9.8	−619.197 027 52	1.349 6968
10.0	−574.306 981 85	1.157 0413
10.2	−530.483 733 64	0.986 425 98
10.4	−488.378 117 53	0.836 692 71
11.0	−375.856 140 24	0.496 352 65
12.0	−238.113 607 14	0.188 385 11

spherical-tensor operators R and S with rank r and s, respectively. The prime on the sums in equation (D1) indicates that the sums exclude the term where both atoms are in the ground state and $b_i = |j_i - 1|, \ldots, j_i + 1$. The energy denominator is negative and does not depend on projection quantum numbers. Finally, ϵ_0 is the vacuum electric permittivity.

The sums in equation (D1) can be rearranged in several steps using appendix VI of reference [32]. As operators d_1 and d_2 commute, we first note that

$$(T_2(d_1, d_2) \cdot C_2)(T_2(d_1, d_2) \cdot C_2) = \sum_k (-1)^k T_k(T_2(d_1, d_2), T_2(d_1, d_2)) \cdot T_k(C_2, C_2) \tag{D3}$$

with $T_{kq}(C_2, C_2) = \langle k0|2200\rangle C_{kq}$ and Clebsch–Gordan coefficient $\langle j_3 m_3 | j_1 j_2 m_1 m_2\rangle$. We omitted the dependence on orientation $\hat{\mathbf{R}}$ of the spherical harmonics for clarity. The right-hand side of equation (D3) is only nonzero for even $k = 0$, 2, or 4. Secondly, we note that

$$T_{kq}(T_2(d_1, d_2), T_2(d_1, d_2)) = 5 \sum_{l_1 l_2} \sqrt{(2l_1 + 1)(2l_2 + 1)} \begin{Bmatrix} 1 & 1 & l_1 \\ 1 & 1 & l_2 \\ 2 & 2 & k \end{Bmatrix} T_{kq}(T_{l_1}(d_1, d_1), T_{l_2}(d_2, d_2)), \tag{D4}$$

where the d_i have been grouped by atom and $l_i = 0$, 1, or 2 and $l_1 + l_2$ is even for a nonzero value of the nine-j symbol

Next, we isolate the sums over projection quantum numbers and labels n in equation (D1). For atom i, we define spherical tensor operators

$$B_{lq}(b, j; i) = \sum_\beta T_{lq} \left(\frac{d_i | nb\beta\rangle}{\langle gj \| d_i \| nb\rangle}, \frac{\langle nb\beta | d_i}{\langle nb \| d_i \| gj\rangle} \right) \tag{D5}$$

with rank $l = 0$, 1, or 2 and $b = |j-1|, \ldots, j+1$. Here, $\langle gj\|d_i\|nb\rangle$ and $\langle nb\|d_i\|gj\rangle$ are reduced matrix elements of the electric dipole moment operator between the atomic ground state and excited state $|nb\beta\rangle$. Crucially, for a ground-state atom we derive that

$$\langle gjm|B_{lq}(b,j;i)|gjm'\rangle = \langle jm|jlm'q\rangle\sqrt{(2b+1)(2l+1)}W(j1j1;bl) \tag{D6}$$

based on the Wigner-Eckart theorem, equation (3.12) of reference [32], and symmetries of the Racah symbol $W(abcd;ef)$. These matrix elements are independent of label n of the excited state, but still depend on its total angular momentum b.

Moreover, using the Wigner–Eckart theorem again, we realize that the m, m', and q dependences of $\langle gjm|B_{lq}(b,j;i)|gjm'\rangle$ are identical to those for the identity operator, atomic angular momentum operator j_q, and dipole operator $T_{2q}(j,j)$ for $l = 0$, 1, and 2, respectively. In fact, we find

$$B_{lq}(b,j;i) = O_{lq}(i)M(b,j) \tag{D7}$$

with rank-l operator $O_{lq}(i) = I, j_{iq}/\hbar$, and $T_{2q}(j_i,j_i)/\hbar^2$ for atom i and $l = 0$, 1, and 2, respectively. Here, $\hbar$ is the reduced Planck constant and the function $M(b,j;l)$ is given by

$$M(b,j;l=0) = (-1)^{b-j+1}\frac{1}{\sqrt{3}}\sqrt{\frac{2b+1}{2j+1}}, \tag{D8}$$

$$M(b,j;l=1) = \frac{(-1)^{b-j}}{2\sqrt{2}}\sqrt{\frac{2b+1}{2j+1}}\frac{2+j(j+1)-b(b+1)}{j(j+1)}, \tag{D9}$$

and

$$M(b,j;l=2) = \sqrt{\frac{2b+1}{2j+1}}\frac{W(j1j1;b2)}{W(j1j1;j2)}\frac{1}{j(j+1)}. \tag{D10}$$

We put everything together to find for two ground-state atoms

$$V_{\rm vdW}(\vec{\mathbf{R}}) = \frac{1}{R^6}\sum_{k=0,2,4}\sum_{l_1l_2}(T_k\left(O_{l_1}(1),O_{l_2}(2)\right)\cdot C_k(\hat{\mathbf{R}}))30\sqrt{\frac{(2l_1+1)(2l_2+1)}{(2j_1+1)(2j_2+1)}}\begin{Bmatrix}1 & 1 & l_1\\ 1 & 1 & l_2\\ 2 & 2 & k\end{Bmatrix}\langle k0|2200\rangle$$
$$\times\sum_{b_1=|j_1-1|}^{j_1+1}\sum_{b_2=|j_2-1|}^{j_2+1}\frac{(-1)^{b_1-j_1}(-1)^{b_2-j_2}}{\sqrt{(2b_1+1)(2b_2+1)}}M(b_1,j_1;l_1)M(b_2,j_2;l_2)h_{b_1b_2}, \tag{D11}$$

where the matrix

$$h_{b_1b_2} = \frac{1}{(4\pi\epsilon_0)^2}{\sum_{n_1n_2}}'\frac{(g_1j_1\|d_1\|n_1b_1)^2(g_2j_2\|d_2\|n_2b_2)^2}{E_{g_1j_1}+E_{g_2j_2}-E_{n_1b_1}-E_{n_2b_2}} \tag{D12}$$

or, equivalently,

$$E_{\rm h}a_0^6{\sum_{n_1n_2}}'\frac{(g_1j_1\|d_1/(ea_0)\|n_1b_1)^2(g_2j_2\|d_2/(ea_0)\|n_2b_2)^2}{(E_{g_1j_1}+E_{g_2j_2}-E_{n_1b_1}-E_{n_2b_2})/E_{\rm h}}$$

is symmetric for homonuclear dimers. Here, e is the elementary charge, $E_{\rm h}$ is the Hartree energy, and a_0 is the Bohr radius. The prime in the sums over labels n_1 and n_2 excludes the case where both atoms are in their ground state and we have introduced the more symmetric reduced matrix elements $(j\|d\|j') = (-1)^{j-j'}(j'\|{\rm d}\|j)^* = \sqrt{2j+1}\langle j\|d\|j'\rangle$ used by, for example, Edmonds in reference [55].

The allowed values for k, l_1, and l_2 and the operators on the first line of equation (D11) lead to the seven spin-tensor operators defined in the main text. The last three lines of equation (D11) correspond to the van-der-Waals coefficients $C_k^{(i)}$. For example, the choice $O_{l_1}(1) = j_1/\hbar$ and $O_{l_2}(2) = j_2/\hbar$ leads to spin-tensor operators $[j_1\otimes j_2]_{k0}/\hbar^2$ with $k = 0$ or 2 in the main text using the $\otimes$ notation of reference [31] for combining spherical tensor operators. This notation is equivalent to the notation used in reference [32]. Further analysis of equation (D11) shows that the operators with the same l_1 and l_2 but different k have related van-der-Waals coefficients as the k dependence is isolated in the nine-j symbol and the Clebsch–Gordan coefficient in the second line. This leads to the relationships between the two spin-tensors with $l_1 = l_2 = 1$ and the three spin-tensors with $l_1 = l_2 = 2$ given in the main text.

Table 6. Atomic transition energies and Einstein A coefficients from exited states of erbium to its $j' = 6$ ground state. Columns labeled ΔE, A, $u(A)$, and j give transition energies, the value and one-standard deviation uncertainty of the Einstein A coefficients, and the total electronic angular momenta j of the excited states, respectively. A reference to the original data is given in columns labeled by 'Ref.'.

$\Delta E/hc$ (cm^{-1})	A (10^6 s^{-1})	$u(A)$ (10^6 s^{-1})	j	Ref.	$\Delta E/hc$ (cm^{-1})	A (10^6 s^{-1})	$u(A)$ (10^6 s^{-1})	j	Ref.
11 401.197	0.006 377	0.001 594 25	5	[57]	23 885.406	1.02	0.06	5	[56]
11 799.778	0.010 76	0.002 69	6	[57]	24 083.166	102	5.	5	[56]
11 887.503	0.015 39	0.003 8475	7	[57]	24 457.139	32.6	1.6	6	[56]
15 185.352	0.1431	0.035 775	5	[57]	24 943.272	220	10.	7	[61]
15 846.549	0.2624	0.0656	7	[57]	25 159.143	40.3	2.1	7	[56]
16 070.095	0.92	0.05	6	[56]	25 162.553	37.6	1.9	5	[56]
16 321.110	0.090 51	0.022 6275	6	[57]	25 268.259	3.59	0.18	6	[56]
17 073.800	0.24	0.06	6	[59]	25 392.779	31.9	1.6	6	[56]
17 157.307	1.17	0.06	7	[56]	25 598.286	15.1	0.8	7	[56]
17 347.860	0.84	0.04	5	[56]	25 681.933	63	3	5	[56]
17 456.383	0.1833	0.045 825	6	[57]	25 880.274	122	6	6	[56]
19 201.343	0.53	0.053	5	[60]	26 237.004	29.0	1.4	6	[56]
19 326.598	0.663	0.165 75	6	[57]	28 026.045	0.59	0.05	5	[56]
19 508.432	0.6392	0.1598	6	[57]	28 053.943	4.33	0.22	6	[56]
21 168.430	1.16	0.06	7	[56]	29 550.807	0.064	0.007	5	[56]
21 392.817	1.26	0.06	5	[56]	29 794.862	0.296	0.025	5	[56]
21 701.885	7.1	0.4	6	[56]	29 894.203	4.10	0.29	5	[56]
22 124.268	0.264	0.019	5	[56]	30 007.369	7.7	1.93	6	[58]
22 583.504	2.55	0.13	6	[56]	30 251.891	1.05	0.08	5	[56]
22 672.766	5.52	0.28	5	[56]	30 380.282	4.3	0.3	5	[56]
23 080.952	0.7405	0.185 125	7	[57]	30 600.160	0.168	0.017	5	[56]
23 311.577	0.4924	0.1231	6	[57]	31 442.927	0.084	0.009	5	[56]
23 447.079	0.6011	0.150 275	5	[57]	32 062.166	0.175	0.027	5	[56]
23 855.654	6.6	0.3	5	[56]	33 485.216	9.6	0.7	5	[56]

Table 7. Some thulium excited atomic eigen energies with respect to its $j' = 7/2$ ground state and oscillator strengths f from the ground state to these excited states. The first column gives the transition energy. The second and third column are the value and one-standard deviation uncertainty of the oscillator strength, respectively. The fourth column gives the total electronic angular momentum j of the excited state. A reference to the original data is given in the last column. Relevant thulium lines for which Einstein A coefficients are available can be found in table 8.

$\Delta E/hc$ (cm^{-1})	f	$u(f)$	j	Ref.
38 342.570	0.001 69	0.003 38	7/2	[63]
39 019.090	0.000 98	0.001 96	9/2	[63]
39 259.920	0.002 62	0.005 25	5/2	[63]
39 580.720	0.008 22	0.016 44	7/2	[63]
39 847.040	0.001 92	0.003 84	7/2	[63]
40 101.720	0.001 21	0.002 42	9/2	[63]

Lists of currently available atomic transition energies $E_{nb} - E_{gj}$ and observed Einstein A coefficients or oscillator strengths f for erbium and thulium atoms are given in tables 6–8 below. The relevant relationships between the reduced matrix elements $(gj\|d\|nb)$ in equation (D12) on the one hand and A and f on the other are

$$A_{nb\to gj} = \frac{4}{3}\frac{E_\mathrm{h}}{\hbar}\alpha^3\left(\frac{E_{nb} - E_{\mathrm{g\,j}}}{E_\mathrm{h}}\right)^3\left|\left(gj\|\frac{d}{ea_0}\|nb\right)\right|^2\frac{1}{2b+1} \tag{D13}$$

and

$$f_{gj,nb} = \frac{2}{3}\frac{E_{nb} - E_{\mathrm{g\,j}}}{E_\mathrm{h}}\left|\left(gj\|\frac{d}{ea_0}\|nb\right)\right|^2\frac{1}{2j+1}, \tag{D14}$$

respectively. Here, α is the fine-structure constant.

For Er_2 atomic transition data or lines from 48 excited states to the ground state are available. The majority of the data is taken from references [56, 57]. References [58, 59] each supply one line, while for two other lines we rely on private communications [60, 61]. For Tm_2 atomic transition data from 65 excited states to the ground state are available. Data have been taken from references [45, 62, 63]. When line strength information of a transition is available from more than one source, the most accurate datum is chosen.

Table 8. Atomic transition energies and Einstein A coefficients from exited states of thulium to its $j' = 7/2$ ground state. Columns labeled ΔE, A, $u(A)$, and j give transition energies, the value and one-standard deviation uncertainty of the Einstein A coefficients, and the total electronic angular momenta j of the excited states, respectively. A reference to the original data is given in columns labeled by 'Ref.'. Relevant thulium lines for which oscillator strengths are available can be found in table 7.

$\Delta E/hc$ (cm^{-1})	A (10^6 s^{-1})	$u(A)$ (10^6 s^{-1})	j	Ref.	$\Delta E/hc$ (cm^{-1})	A (10^6 s^{-1})	$u(A)$ (10^6 s^{-1})	j	Ref.
16 742.237	0.147	0.026 46	7/2	[45]	29 260.590	5.28	0.264	7/2	[62]
16 957.006	0.651	0.032 55	7/2	[62]	29 316.690	9.80	0.49	9/2	[62]
17 343.374	0.388	0.031 04	7/2	[62]	30 082.180	0.089	0.011 57	5/2	[62]
17 613.659	1.30	0.065	9/2	[62]	30 124.020	0.615	0.055 35	7/2	[62]
17 752.634	1.09	0.0545	5/2	[62]	30 302.420	1.61	0.1127	5/2	[62]
18 837.385	2.17	0.1085	9/2	[62]	30 915.020	4.29	0.2145	9/2	[62]
19 548.834	0.241	0.036 15	5/2	[62]	31 431.880	3.82	0.191	5/2	[62]
19 748.543	0.049	0.008 82	9/2	[45]	31 440.540	1.04	0.052	9/2	[62]
19 753.830	0.398	0.031 84	7/2	[62]	31 510.240	15.9	1.272	7/2	[62]
21 120.836	2.0	0.1	7/2	[62]	32 174.490	1.50	0.135	5/2	[62]
21 161.401	0.421	0.021 05	5/2	[62]	32 446.260	17.5	1.225	7/2	[62]
21 737.685	0.518	0.0259	9/2	[62]	32 811.020	16.1	1.127	7/2	[45]
22 791.176	3.71	0.1855	7/2	[62]	33 623.780	21.7	1.085	7/2	[62]
22 929.717	12.0	0.6	5/2	[62]	34 085.200	11.3	1.13	5/2	[62]
23 781.698	24.3	1.215	9/2	[62]	34 297.170	9.44	1.1328	7/2	[62]
23 873.207	64.0	3.2	7/2	[62]	35 026.220	24.2	1.936	5/2	[62]
24 348.692	63.6	3.18	9/2	[62]	35 261.762	1.13	0.2034	5/2	[45]
24 418.018	97.9	4.895	5/2	[62]	37 576.866	0.46	0.0828	9/2	[45]
25 656.019	2.95	0.1475	5/2	[62]	37 711.074	0.38	0.0684	9/2	[45]
25 717.197	37.2	1.86	7/2	[62]	38 120.710	5.2	0.936	9/2	[45]
25 745.117	106	5.3	5/2	[62]	38 128.370	0.62	0.1116	5/2	[45]
26 126.907	2.94	0.147	5/2	[62]	38 433.920	14.9	1.043	5/2	[45]
26 439.491	0.806	0.056 42	7/2	[62]	38 502.000	14.0	0.98	9/2	[45]
26 646.214	17.4	1.392	9/2	[62]	38 696.790	3.5	0.63	5/2	[45]
26 701.325	99.0	4.95	7/2	[62]	39 161.450	36.8	2.576	7/2	[45]
26 889.125	144	7.2	9/2	[62]	39 206.840	2.7	0.486	9/2	[45]
28 024.010	3.80	0.19	9/2	[62]	39 547.310	6.4	1.152	5/2	[45]
28 051.370	8.99	0.4495	5/2	[62]	39 560.410	14.7	1.029	7/2	[45]
28 448.585	1.42	0.071	5/2	[62]	39 768.790	5.29	0.2645	9/2	[62]
28 555.799	0.668	0.040 08	7/2	[62]					

Table 9. Correlation coefficients $r(C_k^{(i)}, C_l^{(j)})$ among four of the seven dispersion coefficients $C_k^{(i)}$ of Er_2 and Tm_2. Their values and uncertainties are given in table 1 of the main text. Coefficients are labeled by rank k and index i following the notation in the main text. Correlation coefficients with the remaining three dispersion coefficients follow from the exact algebraic relationships among the dispersion coefficients.

Homonuclear erbium dimer				
	Correlation coeff.			
$k, i \backslash l, j$	0, 1	2, 1	0, 2	0, 3
0, 1	1.00	−0.38	−0.50	0.32
2, 1	−0.38	1.00	0.37	−1.00
0, 2	−0.50	0.37	1.00	−0.34
0, 3	0.32	−1.00	−0.34	1.00
Homonuclear thulium dimer				
0, 1	1.00	−0.03	0.15	0.05
2, 1	−0.03	1.00	−0.10	−1.00
0, 2	0.15	−0.10	1.00	0.09
0, 3	0.05	−1.00	0.09	1.00

The uncertainties of and correlations among the van-der-Waals coefficients follow from error propagation on equations (D11) and (D12) and are dominated by the uncorrelated uncertainties of the Einstein A coefficients and oscillator strengths. Uncertainties in the transition energies give negligible contributions. Our values for the van-der-Waals coefficients are listed in the table in the main text. Their covariances can be found in table 9 below.

ORCID iDs

Eite Tiesinga https://orcid.org/0000-0003-0192-5585
Svetlana Kotochigova https://orcid.org/0000-0003-0580-3788

References

[1] Griesmaier A, Werner J, Hensler S, Stuhler J and Pfau T 2005 Bose–Einstein condensation of chromium *Phys. Rev. Lett.* **94** 160401
[2] Lahaye T, Menotti C, Santos L, Lewenstein M and Pfau T 2009 The physics of dipolar bosonic quantum gases *Rep. Prog. Phys.* **72** 126401
[3] Lu M, Burdick N Q, Youn S H and Lev B L 2011 Strongly dipolar Bose–Einstein condensate of dysprosium *Phys. Rev. Lett.* **107** 190401
[4] Aikawa K, Frisch A, Mark M, Baier S, Rietzler A, Grimm R and Ferlaino F 2012 Bose–Einstein condensation of erbium *Phys. Rev. Lett.* **108** 210401
[5] Frisch A, Aikawa K, Mark M, Rietzler A, Schindler J, Zupanic E, Grimm R and Ferlaino F 2012 Narrow-line magneto-optical trap for erbium *Phys. Rev.* A **85** 051401(R)
[6] Lu M, Burdick N Q and Lev B L 2012 Quantum degenerate dipolar Fermi gas *Phys. Rev. Lett.* **108** 215301
[7] de Paz A *et al* 2013 Nonequilibrium quantum magnetism in a dipolar lattice gas *Phys. Rev. Lett.* **111** 185305
[8] Baier S, Mark M J, Petter D, Aikawa K, Chomaz L, Cai Z, Baranov M, Zoller P and Ferlaino F 2016 Extended Bose–Hubbard models with ultracold magnetic atoms *Science* **352** 201–5
[9] Natale G, van Bijnen R M W, Patscheider A, Petter D, Mark M J, Chomaz L and Ferlaino F 2019 Excitation spectrum of a trapped dipolar supersolid and its experimental evidence *Phys. Rev. Lett.* **123** 050402
[10] Petrov A, Tiesinga E and Kotochigova S 2012 Anisotropy-induced Feshbach resonances in a quantum dipolar gas of highly magnetic atoms *Phys. Rev. Lett.* **109** 103002
[11] Kotochigova S 2014 Controlling interactions between highly magnetic atoms with Feshbach resonances *Rep. Prog. Phys.* **77** 093901
[12] Frisch A, Mark M, Aikawa K, Ferlaino F, Bohn J L, Makrides C, Petrov A and Kotochigova S 2014 Quantum chaos in ultracold collisions of gas-phase erbium atoms *Nature* **507** 475–9
[13] Maier T *et al* 2015 Emergence of chaotic scattering in ultracold Er and Dy *Phys. Rev.* X **5** 041029
[14] Makrides C, Li M, Tiesinga E and Kotochigova S 2018 Fractal universality in near-threshold magnetic lanthanide dimers *Sci. Adv.* **4** eaap8308
[15] Frisch A *et al* 2015 Ultracold dipolar molecules composed of strongly magnetic atoms *Phys. Rev. Lett.* **115** 203201
[16] Sukachev D, Sokolov A, Chebakov K, Akimov A, Kanorsky S, Kolachevsky N and Sorokin V 2010 Magneto-optical trap for thulium atoms *Phys. Rev.* A **82** 011405
[17] Khlebnikov V A, Pershin D A, Tsyganok V V, Davletov E T, Cojocaru I S, Fedorova E S, Buchachenko A A and Akimov A V 2019 Random to chaotic statistic transformation in low-field Fano–Feshbach resonances of cold thulium atoms *Phys. Rev. Lett.* **123** 213402
[18] Gorokhov L N, Emelyanov A M and Khodeev Y S 1997 Mass-spectroscopic investigation of stability of gaseous molecules of U_2O_2 and U_2 *High Temp.* **12** 1156–8
[19] Pepper M and Bursten B E 1990 *Ab initio* studies of the electronic structure of the diuranium molecule *J. Am. Chem. Soc.* **112** 7803–4
[20] Gagliardi L and Roos B O 2005 Quantum chemical calculations show that the uranium molecule U_2 has a quintuple bond *Nature* **433** 848–51
[21] Knecht S, Jensen H J A and Saue T 2019 Relativistic quantum chemical calculations show that the uranium molecule U_2 has a quadruple bond *Nat. Chem.* **11** 40–4
[22] Buchachenko A A, Chałasiński G and Szczęśniak M M 2007 Interactions of lanthanide atoms: comparative *ab initio* study of YbHe, Yb_2 and TmHe, TmYb potentials *Eur. Phys. J.* D **45** 147–53
[23] Tomza M 2014 *Ab initio* properties of the ground-state polar and paramagnetic europium-alkali-metal-atom and europium-alkaline-earth-metal-atom molecules *Phys. Rev.* A **90** 022514
[24] Dunning A, Petrov A, Schowalter S J, Puri P, Kotochigova S and Hudson E R 2015 Photodissociation spectroscopy of the dysprosium monochloride molecular ion *J. Chem. Phys.* **143** 124309
[25] González-Martínez M L and Żuchowski P S 2015 Magnetically tunable Feshbach resonances in Li + Er *Phys. Rev.* A **92** 022708
[26] Zaremba-Kopczyk K, Żuchowski P S and Tomza M 2018 Magnetically tunable Feshbach resonances in ultracold gases of europium atoms and mixtures of europium and alkali-metal atoms *Phys. Rev.* A **98** 032704
[27] Kosicki M B, Borkowski M and Żuchowski P S 2020 Quantum chaos in Feshbach resonances of the ErYb system *New J. Phys.* **22** 023024
[28] Śmiałkowski M and Tomza M 2021 Highly polar molecules consisting of a copper or silver atom interacting with an alkali-metal or alkaline-earth-metal atom *Phys. Rev.* A **103** 022802
[29] Gomes A S P *et al* 2019 DIRAC, a relativistic *ab initio* electronic structure program, release DIRAC19 http://diracprogram.org
[30] Tecmer P, Boguslawski K, Borkowski M, Żuchowski P S and Kędziera D 2019 Modeling the electronic structures of the ground and excited states of the ytterbium atom and the ytterbium dimer: a modern quantum chemistry perspective *Int. J. Quantum Chem.* **119** e25983
[31] Santra R and Greene C H 2003 Tensorial analysis of the long-range interaction between metastable alkaline-earth-metal atoms *Phys. Rev.* A **67** 062713
[32] Brink D M and Satchler G R 1993 *Angular Momentum* 3rd edn (Oxford: Clarendon)
[33] In the literature quadrupole moments are often defined to be twice $\mathcal{Q}$; the quadrupole operator Q_{2q}, however, has a unique definition. See, for example, section 4.10 of reference [32]
[34] Kotochigova S and Petrov A 2011 Anisotropy in the interaction of ultracold dysprosium *Phys. Chem. Chem. Phys.* **13** 19165
[35] In this section we have implicitly made a change in coordinate system, where R is now the separation between the center of masses of the atoms rather than the separation between the nuclei. Similarly, we use atomic rather than nuclear masses in the kinetic

energy operator. These 'non-adiabatic' changes are not considered significant in light of the uncertainties of our interaction potentials
[36] Colbert D T and Miller W H 1992 A novel discrete variable representation for quantum mechanical reactive scattering via the *S*-matrix Kohn method *J. Chem. Phys.* **96** 1982–91
[37] Knowles P J, Hampel C and Werner H J 1993 Coupled cluster theory for high spin, open shell reference wave functions *J. Chem. Phys.* **99** 5219–27
[38] Dolg M, Stoll H and Preuss H 1989 Energy-adjusted *ab initio* pseudopotentials for the rare earth elements *J. Chem. Phys.* **90** 1730–4
[39] Cao X and Dolg M 2002 Segmented contraction scheme for small-core lanthanide pseudopotential basis sets *J. Mol. Struct.: THEOCHEM* **581** 139–47
[40] Visscher L, Visser O, Aerts P J C, Merenga H and Nieuwpoort W C 1994 Relativistic quantum chemistry: the MOLFDIR program package *Comput. Phys. Commun.* **81** 120–44
[41] Herzberg G 1950 *Molecular Spectra and Molecular Structure. Volume I: Spectra of Diatomic Molecules* (Princeton, NJ: Van Nostrand-Reinhold)
[42] Hougen J T 1970 *The Calculation of Rotational Energy Levels and Rotational Line Intensities in Diatomic Molecules* (*NBS Monograph*) vol 115 (Gaithersburg: National Institute of Standards and Technology) (https://doi.org/10.6028/NBS.MONO.115)
[43] Huang W J, Audi G, Wang M, Kondev F G, Naimi S and Xu X 2017 The AME2016 atomic mass evaluation (I). Evaluation of input data; and adjustment procedures *Chin. Phys.* C **41** 030002
[44] Wang M, Audi G, Kondev F G, Huang W J, Naimi S and Xu X 2017 The AME2016 atomic mass evaluation (II). Tables, graphs and references *Chin. Phys.* C **41** 030003
[45] Kramida A, Ralchenko Y and Reader J (NIST ASD Team) 2019 *NIST Atomic Spectra Database (version 5.7.1)* (Gaithersburg, MD: National Institute of Standards and Technology) (https://dx.doi.org/10.18434/T4W30F)
[46] Stanton J F *et al* 2014 CFOUR, a quantum chemical program package http://cfour.de
[47] Werner H-J *et al* 2015 MOLPRO, version 2015.1, a package of *ab initio* programs https://molpro.net
[48] Akima H 1991 A method of univariate interpolation that has the accuracy of a third-degree polynomial *ACM Trans. Math. Softw.* **17** 341–66
[49] Tao J, Perdew J P and Ruzsinszky A 2012 Accurate van der Waals coefficients from density functional theory *Proc. Natl Acad. Sci.* **109** 18–21
[50] Feller D and Peterson K A 2007 Probing the limits of accuracy in electronic structure calculations: is theory capable of results uniformly better than 'chemical accuracy'? *J. Chem. Phys.* **126** 114105
[51] Kodrycka M and Patkowski K 2019 Platinum, gold, and silver standards of intermolecular interaction energy calculations *J. Chem. Phys.* **151** 070901
[52] Stone A 2013 *The Theory of Intermolecular Forces* 2nd edn (Oxford: Oxford University Press)
[53] Derevianko A, Porsev S G and Babb J F 2010 Electric dipole polarizabilities at imaginary frequencies for hydrogen, the alkali-metal, alkaline-earth, and noble gas atoms *At. Data Nucl. Data Tables* **96** 323–31
[54] Mirahmadi M and Pérez-Ríos J 2021 On the formation of van der Waals complexes through three-body recombination *J. Chem. Phys.* **154** 034305
[55] Edmonds A R 1957 *Angular Momentum in Quantum Mechanics* 3rd edn (Princeton, NJ: Princeton University Press)
[56] Lawler J E, Wyart J-F and Den Hartog E A 2010 Atomic transition probabilities of Er I *J. Phys. B: At. Mol. Opt. Phys.* **43** 235001
[57] Meggers W F, Corliss C H and Scribner B F 1975 *Tables of Spectral-Line Intensities* (*NBS Monograph*) 145 (Washington, DC: National Bureau of Standards) https://nvlpubs.nist.gov/nistpubs/Legacy/MONO/nbsmonograph145p1.pdf
[58] Gorshkov V N and Komarovskii V A 1981 Lifetime of excited levels and oscillator strengths of Er I and Er II spectral lines *Opt. Spectrosc.* **50** 853–7
[59] Komarovskii V A and Smirnov Y M 1993 Transition probabilities for the Er atom *Opt. Spectrosc.* **75** 225–7
[60] Lawler J E 2012 private communication. The $j = 5$ erbium excited state with energy $hc \times 19\,201.343\ \mathrm{cm}^{-1}$ above the ground state has a lifetime of 1700(170) ns and branching ratio of 0.9 to the ground state
[61] Ferlaino F 2012 private communication. The Einstein A coefficient of the $j = 7$ erbium excited state with energy $hc \times 24\,943.272\ \mathrm{cm}^{-1}$ above the ground state has been supplied by the author
[62] Wickliffe M E and Lawler J E 1997 Atomic transition probabilities for Tm I and Tm II *J. Opt. Soc. Am.* B **14** 737–53
[63] Penkin N P and Komarovskii V A 1976 *J. Quant. Spectrosc. Radiat. Transfer* **16** 217-52